Chapter 2
Design Fundamentals of Electrical Machines and Drive Systems

Abstract This chapter presents a brief summary of the design fundamentals including the analysis models and methods for electrical machines and drive systems, based on our design experiences, particularly for permanent magnet electrical machine with soft magnetic composite cores. Because of the multi-disciplinary nature, these design models and methods will be investigated at the disciplinary level, including electromagnetic, thermal, mechanical, power electronics, and control algorithm designs. Several design examples will be presented to illustrate the corresponding design models and methods based on our research findings, such as the finite element model for design analysis of motors, and the model predictive control algorithm and its improvement form for the drive systems. These models and algorithms will be employed in the design optimization of electrical machines and drive systems in the following chapters.

Keywords Electrical drive systems · Electromagnetic design · Thermal design · Mechanical design · Power electronics design · Control algorithms · Finite element model · Model predictive control

2.1 Introduction

2.1.1 Framework of Multi-disciplinary Design

Figure 2.1 illustrates a general framework of multi-disciplinary design for electrical machines and drive systems. As shown, three main components, i.e., motor, power electronics and controller, have to be investigated when designing such electrical drive systems [1, 2]. The main design procedure includes the following steps.

Firstly, define the specifications of the electrical machine and drive system required by a given application, which include the steady state specifications, such as the rated power, speed range, voltage, current, efficiency, power factor (in case of AC machines), volume and cost, and dynamic performances, such as the maximum overshoot, settling time, and stability.

G. Lei et al., *Multidisciplinary Design Optimization Methods for Electrical Machines and Drive Systems*, Power Systems,
DOI 10.1007/978-3-662-49271-0_2

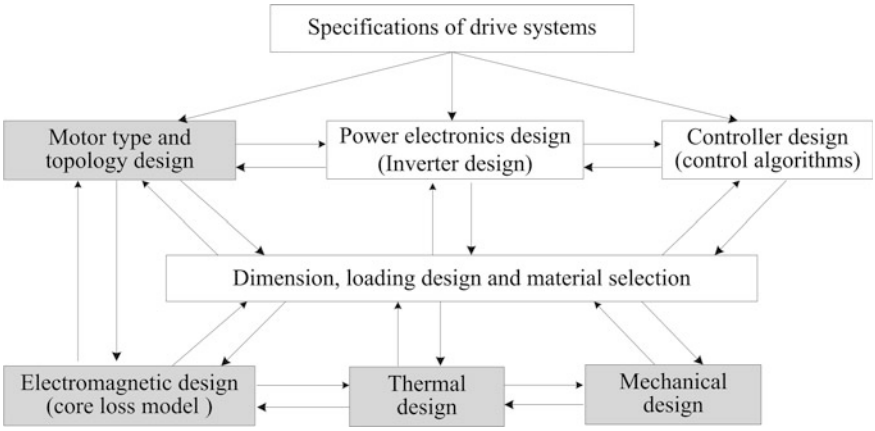

Fig. 2.1 Multi-disciplinary design framework of electrical machines and drive systems

Secondly, select a type of the motor, power electronic converter, and control algorithm from possible options. The motor options include permanent magnet (PM) motors, induction machines, synchronous machines, DC machines, and switched reluctance machines. For servo drives, stepping motors and other types of servo motors can be considered. In this step, different motor topologies have to be investigated as well. The power electronic converter options mainly include the different topologies of AC/DC, DC/DC, and DC/AC converters. The controller design mainly investigates the control strategies and algorithms, such as field oriented control (FOC), direct torque control (DTC), and model predictive control (MPC).

Thirdly, based on the selected motor type, converter circuit, and control scheme, various disciplinary-level analyses should be conducted to evaluate the performance of the drive system. For example, the motor design analysis consists of mainly the electromagnetic, thermal and mechanical analyses (the shaded boxes in the figure). Coupled-field analyses may be required in the design process, such as electromagnetic-thermal and electromagnetic-mechanical stress analyses.

In summary, the design of electrical machines and drive systems mainly consists of the analyses of five coupled disciplines or domains: electromagnetic, thermal, mechanical, power electronics, and controller designs. The following sections will present the popular design analysis models and methods for each discipline.

2.1.2 Power Losses and Efficiency

Power losses and efficiency are two main issues in the design analysis of electrical machines and drive systems. The power losses are mainly composed of the copper loss, core loss, mechanical loss, and stray loss.

(1) The copper loss or Ohmic loss: $P_{\mathrm{Cu}} = I^2R$ is the power dissipated in stator and rotor windings due to the resistance of copper wire, where I is the winding current and R the winding resistance. Normally the DC resistance is used in the calculation. However, it should be noted that the winding resistance depends on the operating conditions, i.e., temperature and frequency (due to the skin effects). In case of the brushes and slip rings/commutator, the effect of contact resistance is often accounted for by assuming a voltage drop of 2 V.

(2) The core loss is the power dissipated in a magnetic core due to the variation of magnetic field. This occurs in the stator and/or rotor iron core of an electrical machine subject to AC excitations. Practically, it can be measured by open-circuit or no-load tests. When the magnetic material is under an alternating sinusoidal flux excitation, the alternating core loss can be calculated by

$$P_a = C_{ha} f B^h + C_{ea}(fB)^2 + C_{aa}(fB)^{1.5} \tag{2.1}$$

where f is the excitation frequency, B the magnitude of sinusoidal magnetic flux density, and C_{ha}, C_{ea}, C_{aa}, and h are the alternating core loss coefficients. In case of rotating electrical machines, the rotational core losses have to be considered. Figure 2.2 plots the average core losses with alternating flux density from 2 to 2,000 Hz and circular rotating flux density vectors from 5 to 1,000 Hz of a cubic soft magnetic composite (SMC) SOMALY$^{\mathrm{TM}}$ 500 sample [3]. These are the standard core loss data used to identify the core loss model parameters. The circularly rotational core loss can be calculated by

$$P_r = P_{hr} + C_{er}(fB)^2 + C_{ar}(fB)^{1.5} \tag{2.2}$$

where

$$\frac{P_{hr}}{f} = a_1 \left[\frac{1/s}{(a_2 + 1/s)^2 + a_3^2} - \frac{1/(2-s)}{[a_2 + 1/(2-s)]^2 + a_3^2} \right]$$

and

$$s = 1 - \frac{B}{B_s}\sqrt{1 - [1/(a_2^2 + a_3^2)]}$$

B_s is the saturation flux density, and C_{er}, C_{ar}, a_1, a_2 and a_3 are the rotational core loss coefficients.

When the material is under a two dimensional elliptically rotating **B** excitation, the core loss can be computed by

$$P_{er} = R_B P_r + (1 - R_B)^2 P_a \tag{2.3}$$

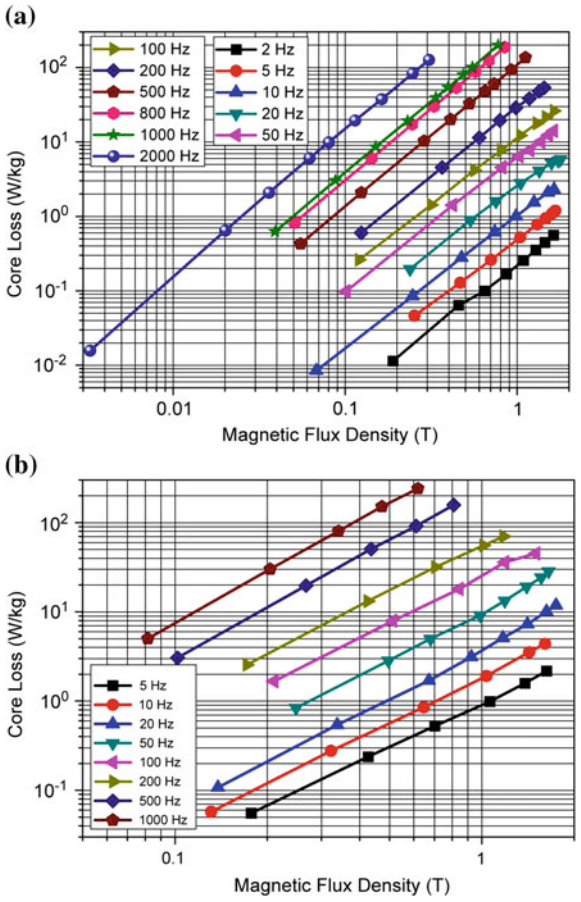

Fig. 2.2 Average core losses under **a** alternating and **b** circular rotating magnetic fluxes [3]

where $R_B = B_{\min}/B_{\text{maj}}$ is the axis ratio, $B_{\min}$ and B_{maj} are the magnitudes of the minor and major axes of the ellipse, respectively, and P_r and P_a the corresponding rotational and alternating core losses when $B = B_{\text{maj}}$. More details about the rotational core losses can be found in [3–9].

(3) The mechanical losses are the power losses caused by the friction (brushes, slip rings/commutator, shaft and bearing), damping, windage, and cooling fan. It can be approximately determined by no-load test. In design, empirical data are used.

(4) The stray loss is the power loss caused by stray factors that are hard to determine separately, such as the non-uniform current distribution in conductors and additional core loss due to distorted magnetic flux distribution for various reasons. Because it is usually difficult to determine accurately the stray loss, estimations based on experimental tests and empirical judgment are

acceptable. For most types of machines, this can be assumed to be 1 % of the output power.

In most electrical machines, the stator and/or rotor cores subject to varying magnetic fluxes are made of laminated silicon steels, which have low core loss, and hence the major power loss is the copper loss. Depending on the type of machine, the copper loss normally accounts for 80–90 % of the total loss.

Based on the above analysis, the efficiency of a machine can be calculated by

$$\eta = \frac{P_{out}}{P_{in}} = \frac{P_{in} - (P_{Cu} + P_{Core} + P_{Mec} + P_{Stray})}{P_{in}} \tag{2.4}$$

Typical values of full load efficiency for rotating machines are:

- 50 % or less for fractional horse power motors (a few W to a few hundreds of W),
- 75–85 % for electrical machines of 1 kW to a few tens of kW,
- 85–95 % for electrical machines of 100 kW to 1 MW, and
- 95–98 % or above for electrical machines of 1 MW to a few hundreds of MW (e.g. 98 % for 100 MVA turbo generator).

2.2 Electromagnetic Design

Since electrical machines are electromagnetic devices for transforming electrical power at one voltage to another (transformers) or converting electric power into mechanical power or vice versa (motors or generators) by the principle of electromagnetic induction, electromagnetic design is a fundamental design stage of electrical machines and drive systems, and is usually based on the following three kinds of analysis models: the analytical model, magnetic circuit model, and finite element model (FEM) [10–20].

2.2.1 Analytical Model

Analytical model is generally used to calculate the performance indicators of electrical machines, such as the output power, torque, and cogging torque. For example, the power and sizing equations are the powerful ways to guide the design of PM motors [10, 11]. By utilizing the current density in the sizing equation, some basic internal relationships can be found among the main dimensions to maximize the torque density.

Assuming the flux linkage of stator winding in a PM motor is sinusoidal, and ignoring the winding resistance, the input power P_{in} can be expressed by

$$P_{in} = \frac{m}{T}\int_0^T e(t)i(t)dt = \frac{m}{T}\int_0^T E_m sin\left(\frac{2\pi}{T}t\right) I_m sin\left(\frac{2\pi}{T}t\right)dt = \frac{m}{2}E_m I_m \tag{2.5}$$

where m is the number of phases, E_m the peak value of back electromotive force (EMF), I_m the peak value of phase current, and T the electrical time period. The output torque can be calculated by

$$T_{out} = \frac{P_{out}}{\omega_r} = \eta\frac{m}{2}p\lambda_p K_{sf} A_s J_m \tag{2.6}$$

where η is the efficiency, p the number of pole pairs, λ_p the peak value of PM flux linkage, ω_r the mechanical rotary speed, K_{sf} the slot fill factor, A_s the slot area, and J_m the peak of current density. For different kinds of PM motors, λ_p and A_s are related differently to their dimensions [21–23].

2.2.2 Magnetic Circuit Model

The magnetic circuit model acts as a uniform principle in descriptive magneto-statics, and as an approximate computational aid in electrical machine design. The model uses the conception of magnetic reluctance to establish an equivalent circuit for approximate analysis of static magnetic field in electrical machines [24]. To illustrate this model, a PM transverse flux machine (TFM) designed by SMC material is investigated.

The SMC material is a relatively new soft magnetic material that has many advantages over the conventional silicon steel sheets. The main advantages of SMC material are the magnetic and mechanical isotropy and low cost, high productivity, and high quality manufacturing capability of complex electromagnetic components by the matured powder metallurgical molding technology, which will enable low cost high productivity commercial manufacturing of SMC motors for a great variety of electrical appliances [24–32].

In our previous work, a 3D flux PM TFM with SMC stator core was developed. Figure 2.3 shows a photo of the PM-SMC TFM prototype. This machine was initially designed to deliver an output power of 640 W at 1800 rev/min. It has 20 poles in the external PM rotor, i.e., 120 PMs in the rotor and 60 SMC teeth in the stator. The stator core is made of SMC SOMALOY^{TM} 500. The operating frequency of this motor is 300 Hz at 1800 rev/min. Table 2.1 tabulates the main design dimensions for this TFM [24, 25].

In order to briefly predict the performance of this TFM, a sketchy magnetic circuit model as shown in Fig. 2.4 can be used. Figure 2.4 illustrates the main flux circuit model and flux path of this TFM, where the resistances represent the magnetic reluctances and the current source (PhiPM) stands for the magneto-motive forces (mmfs) of PMs, and thus R_{ry} represents the magnetic reluctance of rotor, R_m the

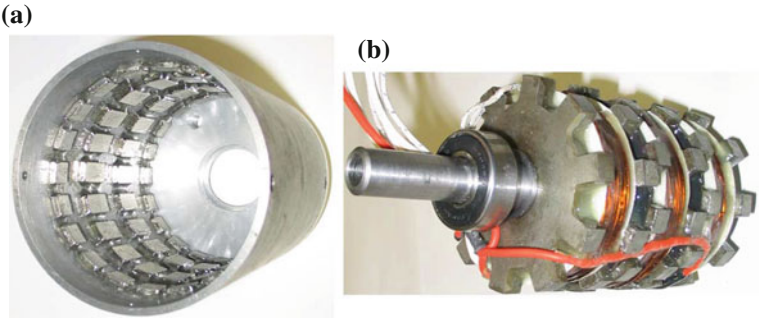

Fig. 2.3 Photo of the PM-SMC TFM prototype, **a** PM rotor, and **b** 3 stack SMC stator

Table 2.1 Main design dimensions of PM-SMC TFM

Par.	Description	Unit	Value
–	Number of phases	–	3
–	Number of poles	–	20
–	Number of stator teeth	–	60
–	Number of magnets	–	120
–	Stator outer radius	mm	40
–	Effective stator axial length	mm	93
x_1	PM circumferential angle	degree	12
x_2	PM width	mm	9
x_3	SMC tooth circumferential width	mm	9
x_4	SMC tooth axial width	mm	8
x_5	SMC tooth radial height	mm	10.5
x_6	Number of turns	–	125
x_7	Diameter of copper wire	mm	1.25
x_8	Air gap length	mm	1.0

magnetic reluctance of PM, R_g the magnetic reluctance of the air gap, R_{st1} the magnetic reluctance of the stator teeth, R_{st2} and R_{sy} stand for the magnetic reluctance of the stator yoke. By analyzing this model, the main magnetic flux can be calculated.

Meanwhile, the magnetic flux leakage is a serious problem in this TFM, thus it should be considered in the magnetic circuit model. Several flux leakage models can be constructed for this TFM. Figure 2.5 illustrates the main flux leakage model. In this model, the adjacent PM in the one side of the machine is modeled, where R_{ry1} represents the magnetic reluctance of rotor, R_{g1} and R_{g2} represent the magnetic reluctance of the air gap, R_{s1} stands for the magnetic reluctance of the stator.

With the computed flux linkage, the resultant magnetic flux density in the air gap and the flux per turn of coil can be estimated. After calculation, the obtained flux per turn of this PM-SMC TFM is 0.32 mWb, which is higher than the calculated result (0.28 mWb) by using the FEM [24].

This model can be also used to evaluate the performance of the motor. Based on the calculated magnetic flux of the motor, the flux linkage per phase equals the

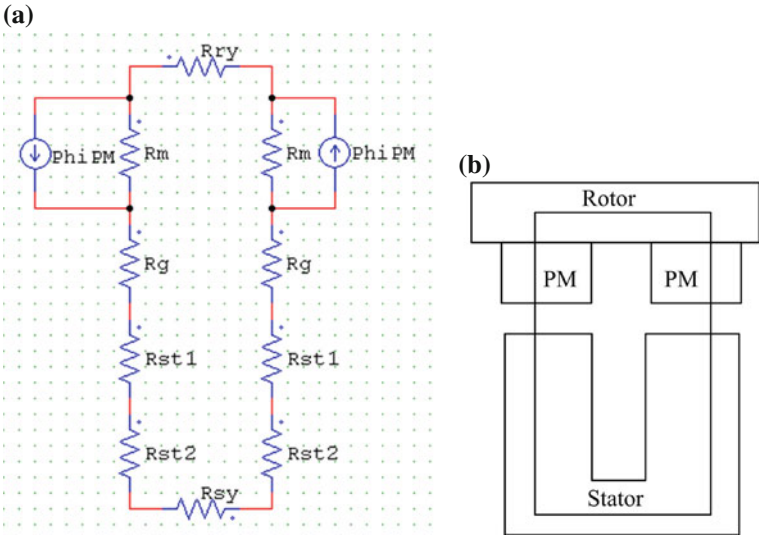

Fig. 2.4 Main flux circuit and flux path of the PM-SMC TFM, **a** magnetic circuit model, **b** flux path in 2D plane

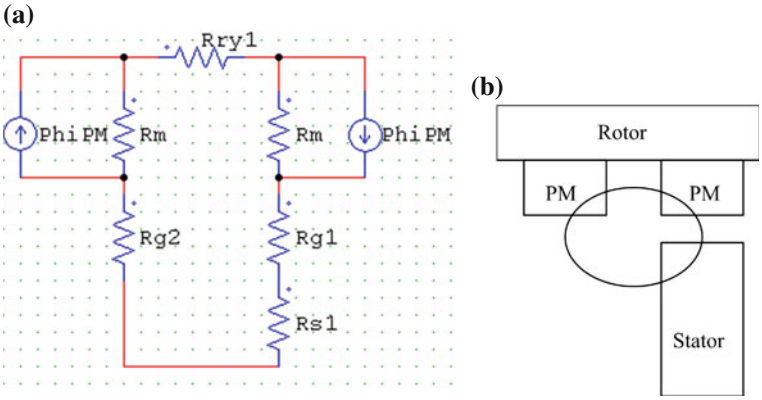

Fig. 2.5 Flux leakage circuit and path of the PM-SMC TFM, **a** magnetic circuit model, **b** leakage path in 2D plane

number of coil turns multiplied by the magnetic flux of each coil turn, and it can be computed as

$$\lambda_{PM} = k_l N_{coil} p \Phi_{gap} \tag{2.7}$$

where λ_{PM} is the PM flux linkage per phase, k_l the leakage coefficient, N_{coil} the number of turns of the phase winding, p the number of pole pairs, and Φ_{gap} is flux per coil turn. The back EMF can be expressed as

$$E_m = \omega_e \lambda_{PM} = p\omega_m \lambda_{PM} \tag{2.8}$$

where $\omega_e = p\omega_m$ is the electrical angular frequency, and ω_m the mechanical angular speed. The electromagnetic torque T_{em} can be expressed as

$$T_{em} = \frac{P_{em}}{\omega_m} = \frac{\sqrt{2}}{2} mp\lambda_{PM} I_m \tag{2.9}$$

After the calculation, the no-load back EMF is 53.26 V at the rated speed of 1800 rev/min. According to (2.9), the electromagnetic torque is 4.66 Nm at the rated current of 5.5 A (RMS value). Compared to the electromagnetic torque obtained from FEM, i.e., 4.08 Nm, the relative error is about 0.58/4.08 = 14.21 %.

2.2.3 Finite Element Model

FEM is a widely used analysis model for field analysis in electrical machines as well as other electromagnetic devices. The theory of FEM can be found in many books and research papers. The PM-SMC TFM investigated above will be employed as an example to show the application of FEM for designing electrical machines.

When analyzing the magnetic field distribution, we used field analysis software package ANSYS, and taking advantage of the periodical symmetry, we only need to analyze one pole-pair region of the machine, as shown in Fig. 2.6a. At the two radial boundary planes, the magnetic scalar potential obeys the periodical boundary conditions:

$$\varphi_m(r, \Delta\theta, z) = \varphi_m(r, -\Delta\theta, z) \tag{2.10}$$

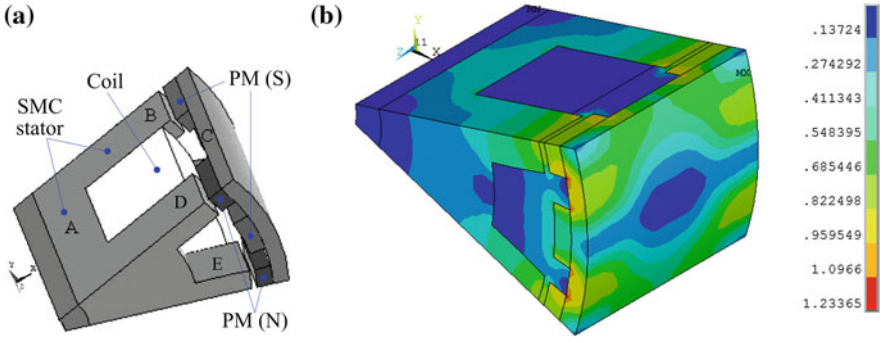

Fig. 2.6 **a** One pole pitch of FEM solution region for one phase (stack), and **b** magnetic field distribution under no-load

Table 2.2 Key PM-SMC TFM parameters

Parameter	Unit	Calculated	Measured
Motor back EMF constant	Vs	0.247	0.244
Phase resistance	Ω	0.310	0.305
Phase inductance	mH	6.68	6.53
Maximal cogging torque	Nm	0.339	0.320

where $\Delta\theta = 18^\circ$ mechanical is the angle of one pole pitch. The origin of the cylindrical coordinate is located at the center of the stack.

Figure 2.6b illustrates the magnetic field distribution under no-load. Based on the FEM analysis, the calculated key motor parameters for this machine are listed in Table 2.2. The measured parameters are also listed in the table to show the effectiveness of the FEM method. As shown, the measured motor back EMF constant is 0.244 Vs, 1 % lower than the calculated value of 0.247 Vs. The calculated phase resistance and inductance, and maximal cogging torque are 0.310 Ω, 6.68 mH and 0.339 Nm, respectively, which are very close to the measured values (0.305 Ω, 6.53 mH and 0.320 Nm). In summary, the estimated parameters calculated by the FEM-based method are well aligned with the experimental results. Therefore, FEM is better than magnetic circuit model, and it is reliable to be used for optimization of the electromagnetic design of electrical machines.

Moreover, the output performance parameters, such as output power, torque and efficiency, can be estimated with the calculated electromagnetic parameters mentioned above. In the estimation, the control method is assumed to maintain that the *d*-axis component of current equals zero. Figure 2.7 shows the per phase equivalent electric circuit of this motor under the assumed control method.

Based on this per phase equivalent electrical circuit, the main relationships of the motor can be predicted by

$$V_{in} = \sqrt{(E_a + I_a R_a)^2 + (\omega_e L_a I_a)^2} \tag{2.11}$$

$$P_{in} = 3V_{in} I_a \cos\varphi \tag{2.12}$$

$$P_{out} = P_{in} - P_{core} - P_{copper} - P_{mech} \tag{2.13}$$

$$T_{out} = \frac{P_{out}}{\omega_r} \tag{2.14}$$

where V_{in} is the input voltage, E_a the back EMF, I_a the armature current, ω_e the electric angular frequency, L_a the inductance, R_a the resistance, φ the angle between V_{in} and E_a, P_{in} the input power, P_{out} the output power, P_{core} the core loss, P_{copper} the copper loss, P_{mech} the mechanical loss, T_{out} the output torque, and ω_r the mechanical angular speed.

In motor with SMC cores, unlike the conventional motors made of silicon sheet steels, the core loss can be a major part among all power losses, and the mechanical

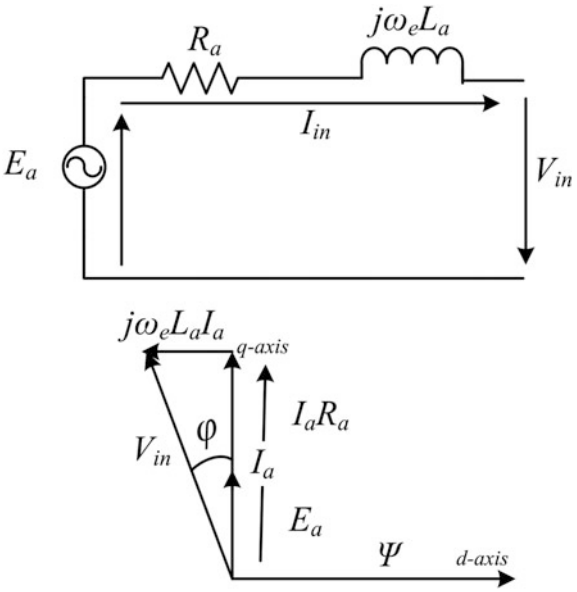

Fig. 2.7 Per phase equivalent electric circuit and phasor diagrams of the motor

loss is generally considered as 1–1.5 % of the output power. In general, the core loss prediction in the TFM should be calculated by using the FEM based on the multi-frequency core loss characteristic of the material. More comparison results can be seen in [24, 25].

2.3 Thermal Design

2.3.1 Thermal Limits in Electrical Machines

The rating of an electrical machine gives its working capability under the specified electrical and environmental conditions. Major factors that determine the ratings are thermal and mechanical considerations. To obtain an economic utilization of the materials and safe operation of the motor, it is necessary to predict with reasonable accuracy the temperature rise of the internal parts, especially in the coils and magnets.

The temperature rise resulted from the power losses in an electrical machine plays a key role in rating the power capacity of the machine, i.e., the amount of power it can convert without being burnt for a specified length of life time. The life expectancy of a large industrial electrical machine ranges from 10 to 50 years or more. In an aircraft or electronic equipment, it can be of the order of a few thousand hours, whereas in a military application, e.g. missile, it can be only a few minutes.

Table 2.3 Classification of electrical insulation materials

Class	Maximum temperature rise (°C)	Materials
O	90	Paper, cotton, silk
A	105	Cellulose, phenolic resins
B	130	Mica, glass, asbestos with organic binder
F	155	Same as above with suitable binder
H	180	Mica, glass, asbestos with silicone binder, silicone resin, Teflon

The operating temperature of a machine is closely associated with its life expectancy because deterioration of the insulation is a function of both time and temperature. Such deterioration is a chemical phenomenon involving slow oxidation and brittle hardening, leading to loss of mechanical durability and dielectric strength. In many cases the deterioration rate is such that the life of the insulation can be expressed as

$$Life\_Time = Ae^{B/T} \tag{2.15}$$

where A and B are constants and T is the absolute temperature. Roughly, it says that for each 10 °C temperature rise exceeding the maximum allowable temperature rise, the life time of insulation is halved.

Insulation materials used in electrical machines are classified by the maximum allowable temperature rise that can be safely withstood. Table 2.3 lists the classification of electrical insulation materials by the IEC (International Electrotechnical Commission).

Generally, there are two kinds of analysis models for thermal analysis in electrical machines, namely the thermal network model and the FEM [14, 15, 20, 25]. The following sections will present examples for the two methods.

2.3.2 Thermal Network Model

Two design examples will be illustrated to show the usage of thermal network model for the thermal analysis of PM-SMC motors. The first one is a TFM, and the second is a high speed claw pole motor.

A. Transverse flux machine

In this study, the temperature rise was calculated by using a hybrid thermal network model with distributed heat sources, as shown in Fig. 2.8.

For high computation accuracy, every part, e.g. the air gap, is divided into two or more segments. The thermal resistances to heat conduction in the following sections are calculated: rotor yoke (R_{ry}), magnets (R_m), glue between magnets and rotor yoke

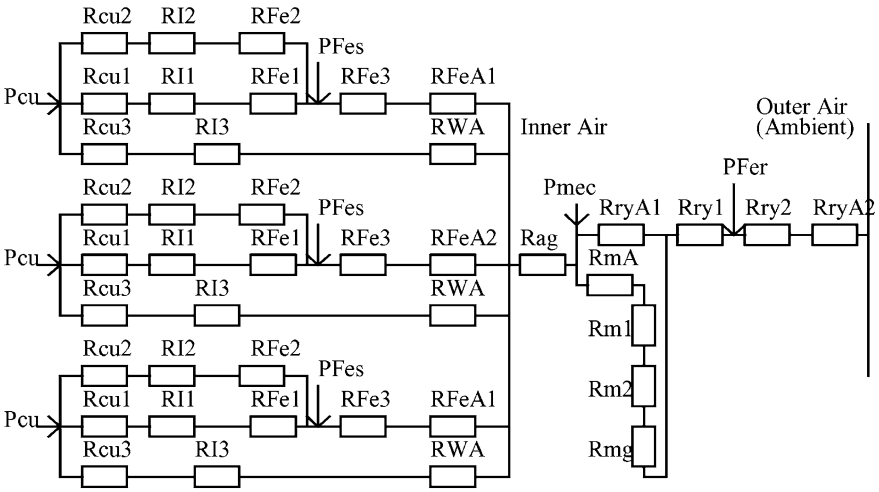

Fig. 2.8 Thermal network model of the TFM prototype

(R_{mg}), air gap (R_{ag}), stator yoke (R_{Fe1}), stator side discs (R_{Fe2}), stator teeth (R_{Fe3}), varnished copper wire (R_{cu}), and insulations (R_{I1}, R_{I2}, R_{I3}) between the winding and the stator yoke, the stator wall disc, and the air gap, respectively. In addition, the thermal resistances of the stator shaft (R_{ss}), the aluminum end plates (R_{al}), and the stationary air (R_{sa}) between the side stator discs and the end plates are calculated separately [25].

The equivalent thermal resistances to the heat convection of the following sections are calculated: that between the stator tooth surface and the inner air in the air gap (R_{FeA}), that between the winding and the inner air (R_{WA}), that between the magnet and the inner air (R_{mA}), that between the rotor yoke and the inner air (R_{ryA1}), and that between the rotor yoke and the outer air (R_{ryA2}).

The heat sources include the stator winding copper losses (P_{cu}), the stator and rotor core losses (P_{Fes}, P_{Fer}), and the mechanical losses due to windage and friction (P_{mec}). The improved method for core loss calculation can obtain the loss distribution, which is a great advantage for thermal calculation by the hybrid thermal model.

The temperature rises in the middle of several parts are calculated as 64.9 °C in the stator winding, 78.6 °C in the stator core, 59.3 °C in the air gap, 36.1 °C in the magnets, and 25.3 °C in the rotor yoke outer surface. The experimentally measured results are 66 °C in the stator winding and 27 °C in the rotor yoke, and it can be seen that the maximum relative error between the calculated and measured results is only 3 %. Thus, it is reliable to use the thermal network method for design of this TFM.

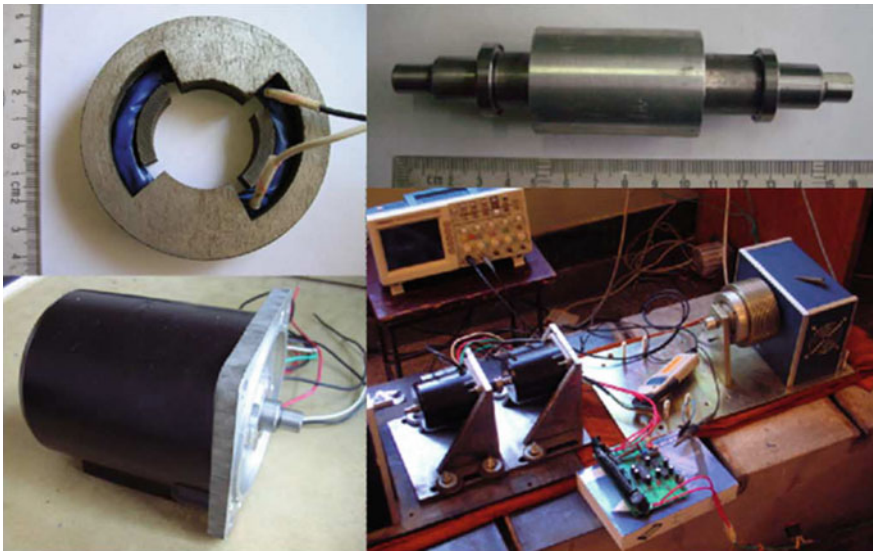

Fig. 2.9 Prototype of a high speed claw pole motor

B. High speed claw pole motor

In our previous work, a high speed claw pole motor as shown in Fig. 2.9 with an SMC stator core was developed [3, 8, 9]. The major motor parameters are tabulated in Table 2.4, and the structure (one pole pitch of one stack) is shown in Fig. 2.10.

Figure 2.11 illustrates the topology of one of the three stacks. The stator consists of the claw poles, the yoke, and the phase winding. The rotor is simply made of a ring PM magnetized in four poles and mounted on the rotor core. The three stator stacks are shifted for 120° (electrical) apart from each other.

Table 2.4 Main dimensions and design parameters

Parameter	Unit	Value
Number of phases	–	3
Rated power	W	2000
Rated frequency	Hz	666.7
Rated speed	rev/min	20,000
Number of poles	–	4
Stator outer diameter	mm	78
Rotor outer diameter	mm	29
Rotor inner diameter	mm	18
Airgap length	mm	1
Axial length	mm	48
Stator core material	–	SOMALOY™ 500
PM material	–	NdFeB

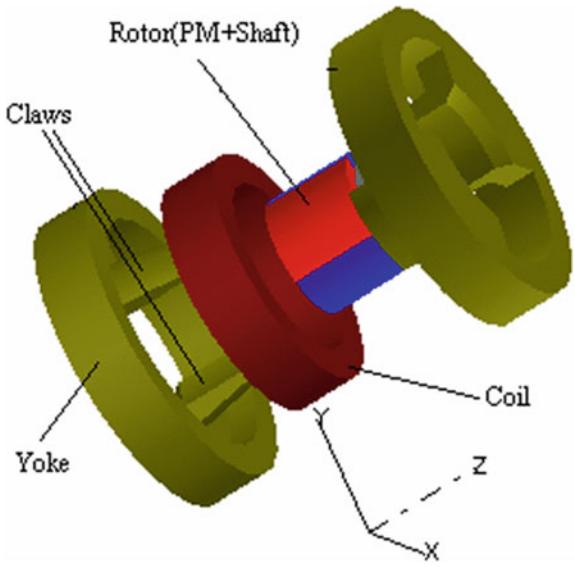

Fig. 2.10 Magnetically relevant parts of one stack of three-phase claw pole motor

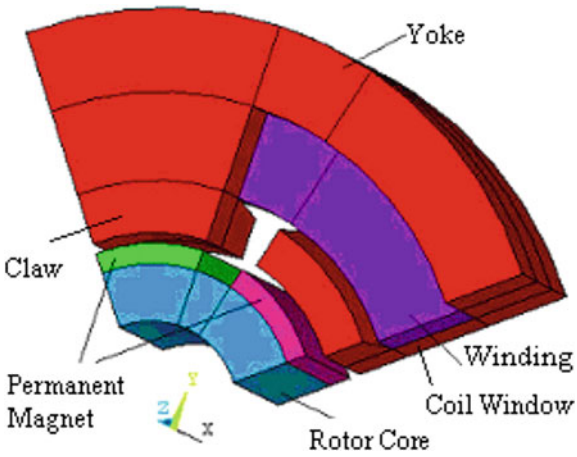

Fig. 2.11 Structure of a high-speed claw pole motor (one pole pitch of one stack)

In general, the geometrical complexity of an electrical machine requires a large thermal network if a high resolution of temperature distribution is required. Instead of using a whole model, the geometrical symmetries of the machine can be used to reduce the size of the model. The distributed thermal properties have been lumped together to form a small thermal network, representing the whole machine. For the calculation of temperature distribution in the SMC motor, a thermal resistance network, as shown in Fig. 2.12, is used. It has ten nodes (the outer air, frame, yoke, and so on). Each node represents a specific part or region of the machine, and the thermal resistances (R_n, $n = 1,\ldots,16$) between the nodes include complex processes,

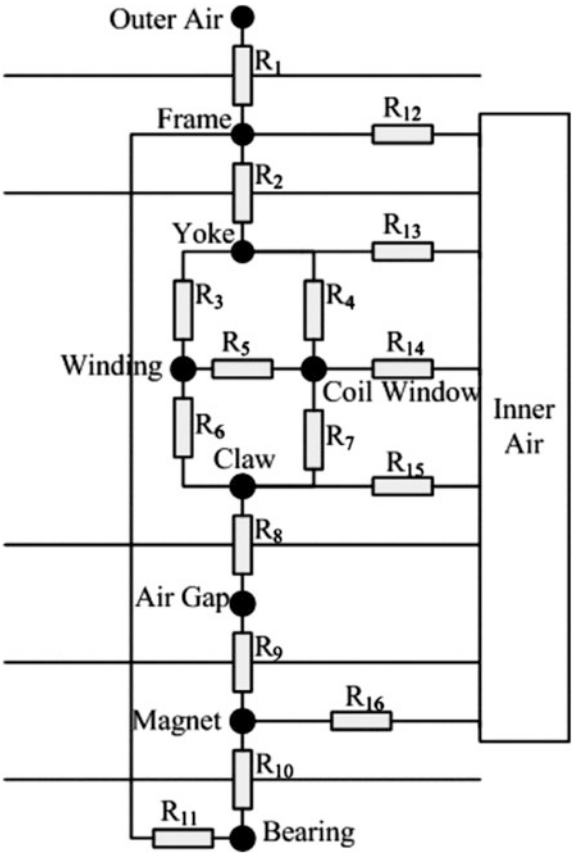

Fig. 2.12 Thermal network of one stack of a high-speed claw pole motor

such as the 2D and 3D heat flow, convection, internal heat generation, and variations in material properties. To account for the three dimensional heat flows at a node, the thermal structure shown in Fig. 2.13 can be employed.

As shown in Fig. 2.13, the thermal resistances of an element are built in three directions, and the heat source if any can be placed at the center point. In this model, the thermal conduction equation can be expressed as

$$\frac{T_b - T_a}{R_{ab}} + \frac{T_c - T_a}{R_{ac}} + \frac{T_d - T_a}{R_{ad}} + \frac{T_e - T_a}{R_{ae}} + \frac{T_f - T_a}{R_{af}} + \frac{T_g - T_a}{R_{ag}} + q_a = C_a \frac{\partial (T_a^{'} - T_a)}{\partial t} \tag{2.16}$$

where T_a, T_b, T_c, T_d, T_e, T_f, and T_g are the temperatures at nodes a, b, c, d, e, f, and g, R_{ab}, R_{ac}, R_{ad}, R_{ae}, R_{af}, and R_{ag} the thermal resistance between nodes a-b, a-c, a-d, a-e, a-f, and a-g, respectively, q_a is the heat source, C_a the heat specific, and $T_a^{'}$ the

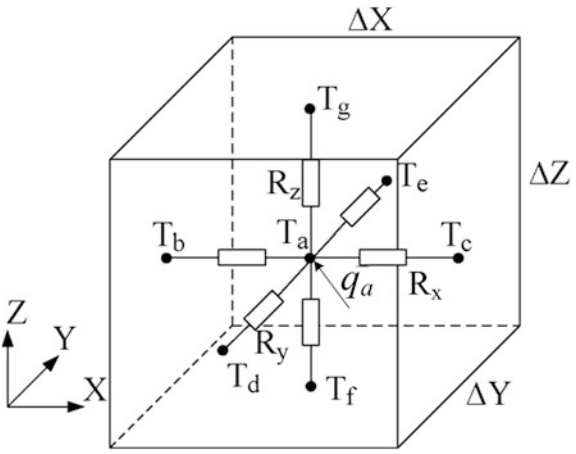

Fig. 2.13 Nodal thermal structure for 3D heat flow

temperature of node a at the next time instant. The thermal resistance in Fig. 2.13 can be calculated by

$$R_{ab} = R_{ac} = \frac{\Delta X}{2\lambda_x \Delta Y \Delta Z} \tag{2.17}$$

$$R_{ad} = R_{ae} = \frac{\Delta Y}{2\lambda_y \Delta X \Delta Z} \tag{2.18}$$

$$R_{af} = R_{ae} = \frac{\Delta Z}{2\lambda_z \Delta X \Delta Y} \tag{2.19}$$

where λ_x, λ_y and λ_z are the thermal conductivities in the x, y and z directions, respectively [8].

The calculation results at no load are 324.6 K in the frame, 326.3 K in the yoke, 330.8 K in the winding, 337.7 K in the claw poles, 334.4 K in the air gap, 331 K in the magnets, and 324.7 K in the bearing.

2.3.3 Finite Element Model

In the thermal network, the core loss at each node cannot be obtained easily from the magnetic field calculation. In most cases, the average value is used. Since the core loss distribution is quite different in different positions of the stator core, 3D FEM is used to analyze the temperature distribution in this section. Two design examples investigated in the previous section will be illustrated to show the usage of FEM for the thermal analysis of PM-SMC motors.

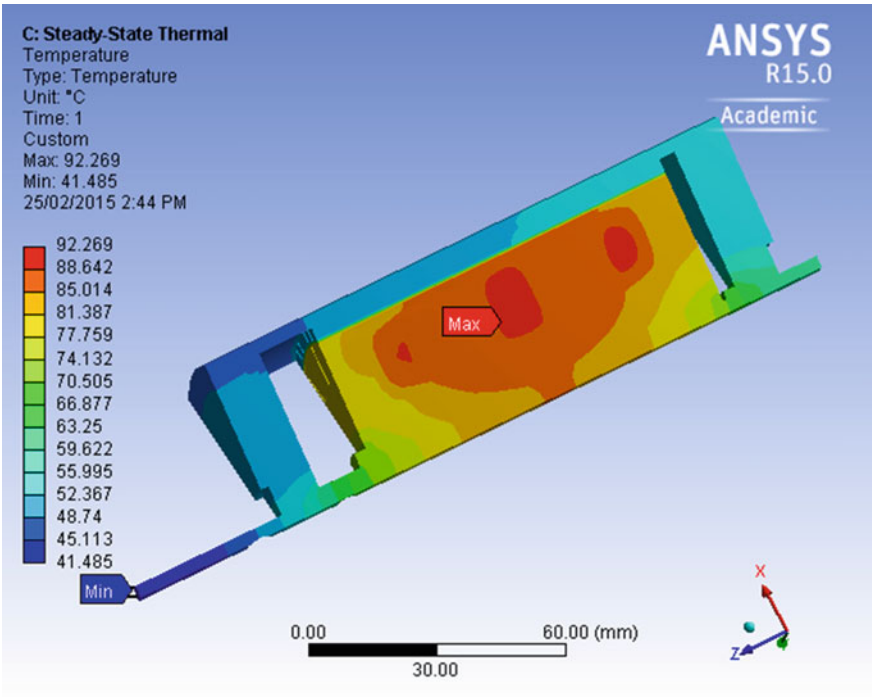

Fig. 2.14 Temperature distribution in the PM-SMC TFM obtained by 3D FEM

Figure 2.14 illustrates the temperature distribution of the PM-SMC TFM based on FEM. As shown, the average temperature rises in the winding is 62.5 °C, which is close to the measured value 65 °C.

Figure 2.15 depicts the distributions of core loss and temperature at full load in the SMC core of the high speed claw pole motor. The temperature is measured by an infrared temperature probe. At 20,000 rev/min and no load, the frame temperature is 331.4 K and the stator yoke temperature is 333.5 K, respectively. The

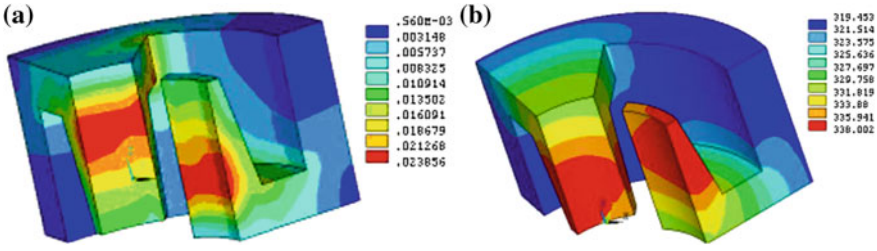

Fig. 2.15 **a** Distributions of core loss, and **b** temperature in SMC core of the high speed claw pole motor

measured temperatures are slightly higher than the FEM results, because the actual loss is greater than the calculation. The FEM method is more accurate than the thermal network method because there are only ten nodes in the network. The advantage of the thermal network is the calculation speed, which is much faster than the FEM method [8, 9].

2.4 Mechanical Design

Mechanical design is another important issue in the design analysis of electrical machines, especially for high speed motors. Generally, the following three aspects should be investigated for the mechanical design analysis:

(1) Mechanical structures and materials,
(2) Field of stress and material strength (including elastic and plastic deformations), and
(3) Modal analysis for vibration and noise.

The first and the second aspects are often noncritical and can be readily satisfied through empirical design, whereas the third one requires special attention for most situations, especially those operated at high frequencies. The modal analysis is generally used to calculate the resonance frequency of the motor in operation. Enough distance between this frequency and the electromagnetic frequency should be designed for motors to avoid resonance. The modal analysis is generally conducted by using the FEM. The two design examples used in the previous section will be employed as follows.

The PM-SMC TFM is operated at 300 Hz, which is relatively high compared with the conventional motors operated at the power frequency of either 50 or 60 Hz. From experience, we only need to do the first-order modal analysis and compare the frequency with the electromagnetic frequency [20]. Figure 2.16 illustrates the first-order modal analysis for this motor of the electromagnetic optimized design. It can be seen that the resonance frequency of the optimal motor is about 4,435 Hz, which is much higher than the electromagnetic frequency of 300 Hz.

Regarding the high speed claw pole motor, because it is operated at high speed, it is essential to carry out a modal analysis to find and adjust the resonant points, so that in practical operation, these frequencies can be avoided. Figure 2.17 shows the vibration patterns and the corresponding resonant frequencies of the rotor structure. These frequencies are well above the operating frequency and therefore have almost no influence to the practical operation. Through the analysis and adjustment, it was found that the bearing stiffness, the shaft length, the shaft diameter and the position of bearing have significant influence on the rotor natural frequency [3].

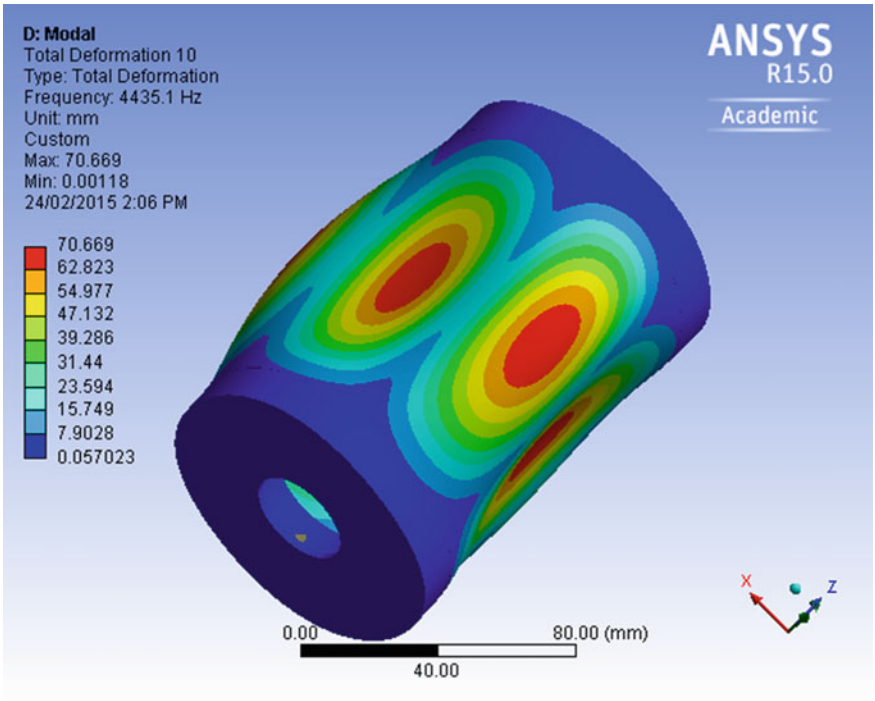

Fig. 2.16 Illustration of first order modal analysis for PM-SMC TFM

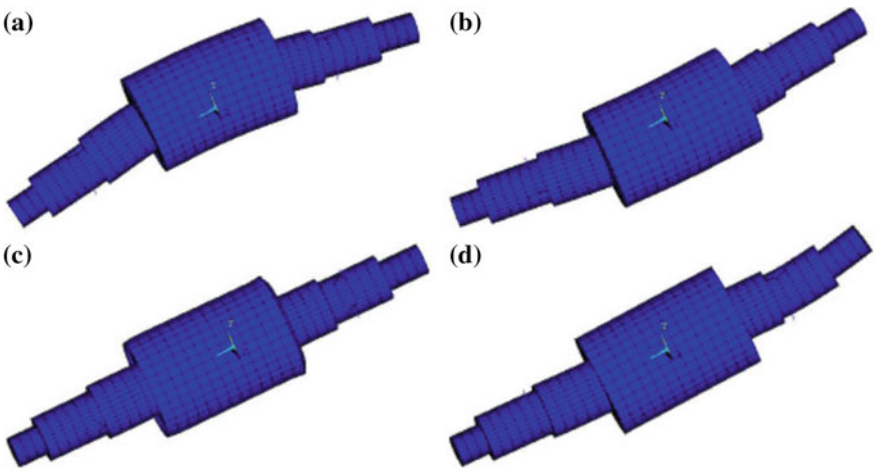

Fig. 2.17 Vibration patterns at **a** 4,102 Hz (Y axis), **b** 4,102 Hz (X axis), **c** 9,562 Hz (Z axis), and **d** 10,321 Hz (Y axis)

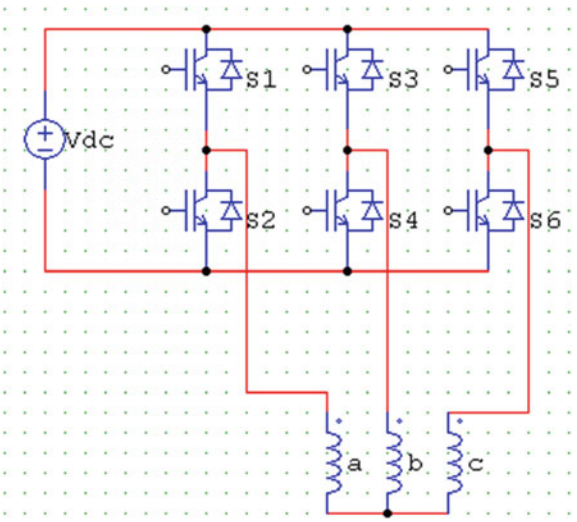

Fig. 2.18 A three-phase inverter

2.5 Power Electronics Design

The design of power electronics for electrical machines and drive systems is also an important and complex stage. Among many aspects in power electronics, the converter/inverter and switching scheme are two main concerns in the design of electrical machines and drive systems.

The converter/inverter is an important component to drive an electrical machine. An inverter, for example, is an electronic apparatus that can convert a DC voltage to an AC voltage of specified waveform, frequency, magnitude, and phase angle. Among many different topologies, the three phase bridge power circuit as shown in Fig. 2.18 has become favorite and standard for use in the control systems of electrical machines. Many different topologies can be obtained from this structure for different applications. For example, two extra switches can be added to establish two bridges for the fault tolerant control scheme [33, 34].

For controlling the waveform, frequency, magnitude, and phase angle of the AC voltage, many switching schemes can be used, such as square wave and sine wave pulse width modulations (PWMs) and space vector modulation (SVM), as well as hard and soft switching.

2.6 Control Algorithms Design

Control algorithms play an important role in the determination of dynamic and state-state performances of electrical drive systems. Various control algorithms have been developed and employed successfully in commercial drive systems, such as the six-step control, FOC, DTC and MPC [35–39].

While FOC is commonly used in various high performance electrical drive system, the merits of DTC are simple in structure (thus low cost), fast dynamic response, and strong robustness against motor parameter variation [40–42]. The major advantages that affect the commercial application of the conventional DTC are large torque and flux ripples, variable switching frequency, and excessive acoustic noises.

To overcome these problems, many methods have been proposed in the literature. One of them is to apply the technique of SVM to DTC, known as the SVM-DTC. In the conventional DTC, the switching table only includes a limited number of voltage vectors with fixed amplitudes and positions. The implementation of SVM enables the generation of an arbitrary voltage vector with any amplitude and position [43–48]. In this way, the SVM-DTC can generate the torque and flux more accurately to eliminate the ripples. Another merit of SVM-DTC is that the sampling frequency required is constant and lower than that of the conventional DTC.

Recently, the MPC has attracted increasing attention in industry and academic communities [49–54]. In the SVM-DTC, the power converter with modulation can be considered as a gain in controller design. In the predictive control methods, the discrete nature of power converters is taken into account by considering the converter and the motor from a systemic viewpoint. There are various different versions of predictive control algorithms, differing in the principle of vector selection, number of the applied vectors and predictive horizon.

The conventional DTC and MPC are similar in that they both select only one voltage vector in each sampling period. This can result in overregulation, leading to large torque and flux ripples and acoustic noise.

As all the design examples used in this book are permanent magnet synchronous machines (PMSMs), several control algorithms will be presented with details for PMSMs in the following sections. Numerical and experimental examples will be presented for some of them.

2.6.1 Six-Step Control

The six-step control method was oriented to drive brushless DC (BLDC) motors with trapezoidal back EMF waveforms. In many applications, however, the trapezoidal excitation is also used to drive PMSMs with sinusoidal back EMF waveforms because the trapezoidal excitation or six-step method based drive is robust and low cost [35].

In the six-step control scheme, the stationary reference frame is always used to model the PMSM. The phase variables are used to express the machine equations as they can account for the real waveforms of the back EMF and phase current. Assuming that the resistances of three phase stator windings are equal, the three phase voltage equations of the motor can be written as

$$\begin{bmatrix} v_a \\ v_b \\ v_c \end{bmatrix} = \begin{bmatrix} R_s & 0 & 0 \\ 0 & R_s & 0 \\ 0 & 0 & R_s \end{bmatrix} \begin{bmatrix} i_a \\ i_b \\ i_c \end{bmatrix} + \frac{d}{dt} \left\{ \begin{bmatrix} L_{aa} & L_{ba} & L_{ca} \\ L_{ba} & L_{bb} & L_{cb} \\ L_{ca} & L_{cb} & L_{cc} \end{bmatrix} \begin{bmatrix} i_a \\ i_b \\ i_c \end{bmatrix} \right\} + \begin{bmatrix} e_a \\ e_b \\ e_c \end{bmatrix} \tag{2.20}$$

where v_a, v_b, and v_c are the phase voltages, i_a, i_b, and i_c the phase currents, e_a, e_b, and e_c the phase back EMF, R_s is the phase resistance, and $\begin{bmatrix} L_{aa} & L_{ba} & L_{ca} \\ L_{ba} & L_{bb} & L_{cb} \\ L_{ca} & L_{cb} & L_{cc} \end{bmatrix}$ the inductance matrix, including both the self-and mutual-inductances.

Assuming further that the reluctance is independent of the rotor position, one can obtain

$$\begin{cases} L_a = L_b = L_c = L_s \\ L_{ab} = L_{ca} = L_{bc} = M \end{cases} \tag{2.21}$$

As $i_a + i_b + i_c = 0$ for a symmetric three phase system, the voltage equation can be simplified as

$$\begin{bmatrix} v_a \\ v_b \\ v_c \end{bmatrix} = \begin{bmatrix} R_s & 0 & 0 \\ 0 & R_s & 0 \\ 0 & 0 & R_s \end{bmatrix} \begin{bmatrix} i_a \\ i_b \\ i_c \end{bmatrix} + \frac{d}{dt} \left\{ \begin{bmatrix} L-M & 0 & 0 \\ 0 & L-M & 0 \\ 0 & 0 & L-M \end{bmatrix} \begin{bmatrix} i_a \\ i_b \\ i_c \end{bmatrix} \right\} + \begin{bmatrix} e_a \\ e_b \\ e_c \end{bmatrix} \tag{2.22}$$

Assuming linear system, the machine model in state space form can be expressed as

$$\frac{d}{dt} \begin{bmatrix} i_a \\ i_b \\ i_c \end{bmatrix} = \begin{bmatrix} 1/(L-M) & 0 & 0 \\ 0 & 1/(L-M) & 0 \\ 0 & 0 & 1/(L-M) \end{bmatrix} \left\{ \begin{bmatrix} v_a \\ v_b \\ v_c \end{bmatrix} - \begin{bmatrix} R_s & 0 & 0 \\ 0 & R_s & 0 \\ 0 & 0 & R_s \end{bmatrix} \begin{bmatrix} i_a \\ i_b \\ i_c \end{bmatrix} - \begin{bmatrix} e_a \\ e_b \\ e_c \end{bmatrix} \right\} \tag{2.23}$$

The generated electromagnetic torque is given by

$$T_e = (e_a i_a + e_b i_b + e_c i_c)/\omega_m \tag{2.24}$$

where ω_m is the mechanical angular speed of the rotor.

The mechanical equation of the machine is

$$T_e = \frac{d\omega_m}{dt} J + F\omega_m + T_L \tag{2.25}$$

where J is the inertia of the machine rotating parts, F the friction coefficient, and T_L the load torque on the rotor shaft.

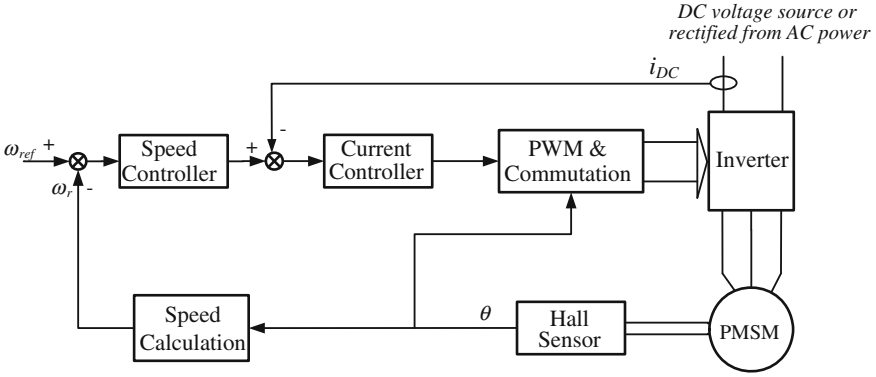

Fig. 2.19 Block diagram of PMSM six-step drive system

Figure 2.19 shows the block diagram of six-step drive scheme. The drive system is operated with the feedback information of rotor position, which is obtained at fixed points, typically every 60 electrical degrees for commutation of the phase currents.

The 120° conduction mode is applied to drive the PMSM. The voltage may be applied to the motor every 120° (electrical), with a current limit to hold the phase currents within the motor's capabilities. Because the phase currents are excited in synchronism with the back EMF, a constant torque is generated. A simulation model is built in MATLAB/SIMULINK as shown in Fig. 2.20.

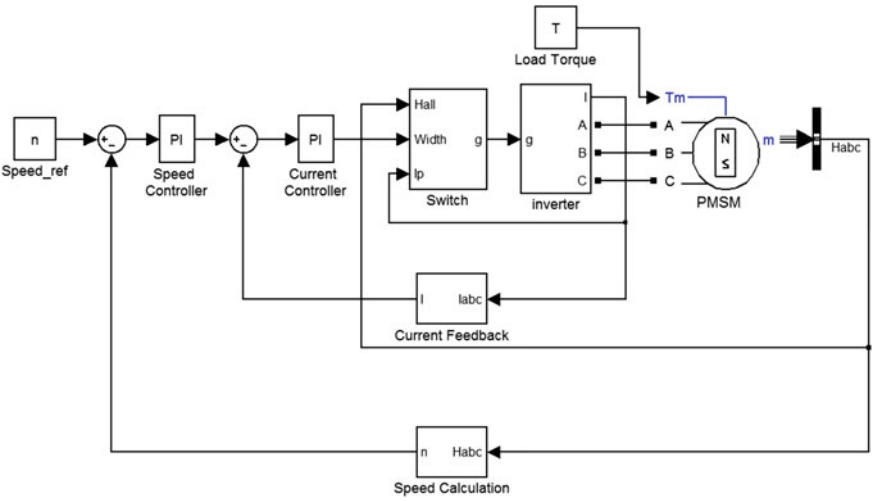

Fig. 2.20 Simulation block diagram of six-step controlled PMSM drive system

As shown in Fig. 2.20, the rotor position information comes from the Hall effect sensors, which are integrated in the machine model in MATLAB/SIMULINK. The resolution of the feedback signals is only 60° (electrical). Since most applications require a stable speed, a speed feedback loop is employed. The rotor speed information can be deduced from the low resolution Hall signals, which is marked as Speed Calculation in Fig. 2.20. Typically, the average speed in one 60° section is used as the speed feedback.

However, by using the average speed, there is always a lag when the motor speed is not constant in accelerating or other dynamic state. To overcome this, the rotor position can be expressed in Taylor's series as the following:

$$\theta(t) = \theta_k(t) + \theta_{1k}^{(1)}(t - t_k) + \frac{\theta_{2k}^{(2)}}{2!}(t - t_k)^2 + \cdots \tag{2.26}$$

where t_k is the last commutation time, $\theta_{1k}^{(1)} = \frac{\pi/3}{t_k - t_{k-1}}$ the average speed of last section, and $\theta_{2k}^{(2)} = \frac{\theta_{1k}^{(1)} - \theta_{1(k-1)}^{(1)}}{t_k - t_{k-1}}$ the average acceleration of last section.

As shown above, with the higher order calculation, more accurate speed and position information can be deduced, whereas the computing cost rises. As a compromise, in some situations, the following equations are used to estimate the rotor position and speed:

$$\begin{cases} \theta(t) = \theta_k(t) + \theta_{1k}^{(1)}(t - t_k) + \frac{\theta_{2k}^{(2)}}{2!}(t - t_k)^2 \\ \omega(t) = \theta_{1k}^{(1)}(t) + \theta_{2k}^{(2)}(t - t_k) \end{cases} \tag{2.27}$$

2.6.2 *Field Oriented Control*

For a PMSM under sinusoidal excitations, the original voltage equations can be expressed in the stationary reference frame as the following

$$\begin{bmatrix} v_a \\ v_b \\ v_c \end{bmatrix} = R_s \begin{bmatrix} i_a \\ i_b \\ i_c \end{bmatrix} + \frac{d}{dt} \begin{bmatrix} \lambda_a \\ \lambda_b \\ \lambda_c \end{bmatrix} \tag{2.28}$$

where λ_a, λ_b, and λ_c are the flux linkages of phases a, b, and c, respectively.

Equation (2.28) represents a system of differential equations with time varying (periodic) coefficients. For sinusoidally distributed windings, a Park-Clark transformation can be used to transform the above equations to a system of differential equations with constant coefficients, represented in a d-q coordinate frame attached to the rotor. The reference frames are shown in Fig. 2.21.

The Park-Clark orthogonal transformation can be expressed in the matrix form as

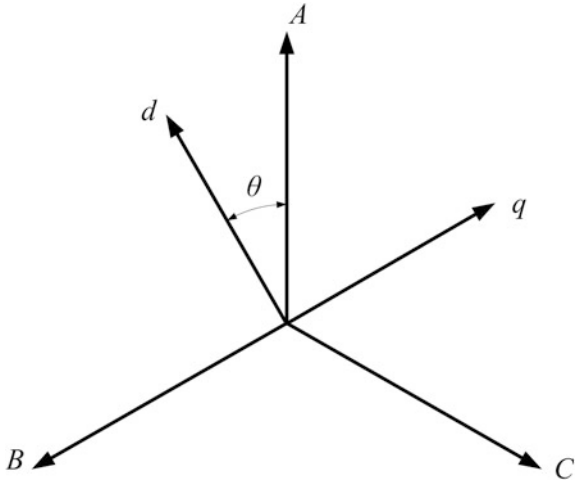

Fig. 2.21 Stationary and rotating reference frames

$$\begin{bmatrix} \sigma_d \\ \sigma_q \\ \sigma_0 \end{bmatrix} = \sqrt{\frac{2}{3}} \begin{bmatrix} \cos\theta & \cos\left(\theta - \frac{2}{3}\pi\right) & \cos\left(\theta + \frac{2}{3}\pi\right) \\ -\sin\theta & -\sin\left(\theta - \frac{2}{3}\pi\right) & -\sin\left(\theta + \frac{2}{3}\pi\right) \\ \frac{1}{\sqrt{2}} & \frac{1}{\sqrt{2}} & \frac{1}{\sqrt{2}} \end{bmatrix} \begin{bmatrix} \sigma_a \\ \sigma_b \\ \sigma_c \end{bmatrix} \tag{2.29}$$

where θ is defined as the angle between two reference frames.

The subscripts d, q, and 0 in (2.29) represent some fictitious windings attached to the rotor. The variables σ_d, σ_q, σ_0, σ_a, σ_b, and σ_c may represent voltages, currents, or flux linkages. As a result, the transformed set of electrical equations describing the behavior of PMSM in the d-q rotating frame become

$$\begin{cases} v_d = R_s i_d + \frac{d}{dt}\lambda_d - \lambda_q \frac{d\theta}{dt} \\ v_q = R_s i_q + \frac{d}{dt}\lambda_q + \lambda_d \frac{d\theta}{dt} \\ v_0 = R_s i_0 + \frac{d}{dt}\lambda_0 \end{cases} \tag{2.30}$$

where v_d, v_q, and v_0 are the phase voltages, i_d, i_q, and i_0 the phase currents, and λ_d, λ_q, and λ_0 the phase flux linkages.

For the linear PMSM model, the magnetic saturation saliency is not considered. The flux linkages of the d- and q-axes can be further expressed as

$$\begin{cases} \lambda_d = L_d i_d + \lambda_m \\ \lambda_q = L_q i_q \end{cases} \tag{2.31}$$

where L_d and L_q are the constant d- and q-axes inductances, respectively, and λ_m is the flux linkage generated by the rotor PMs.

On the other hand, the voltage equation of the 0 axis in (2.30) is usually ignored by assuming well-balanced three-phase windings for the controller design.

Therefore, the electrical voltage equations in the rotor reference frame can be rewritten as

$$\begin{cases} v_d = R_s i_d + L_d \frac{di_d}{dt} - L_q i_q \frac{d\theta}{dt} \\ v_q = R_s i_q + L_q \frac{di_q}{dt} + (L_d i_d + \lambda_m) \frac{d\theta}{dt} \end{cases} \tag{2.32}$$

The torque expression after the application of the transformation becomes

$$\begin{aligned} T_e &= \frac{3}{2} p \left(\lambda_d i_q - \lambda_q i_d \right) \\ &= \frac{3}{2} p \left[\lambda_m i_q + \left(L_d - L_q \right) i_d i_q \right] \end{aligned} \tag{2.33}$$

where p is the number of pole pairs.

By this transformation, the flux and torque control of the PMSM are decoupled. The q-axis current, in the FOC method, is regulated to produce sufficient torque while the d-axis current is controlled to modify the air-gap flux linkage. For normal operation, the d-axis current is set to zero to achieve the maximum torque-to-ampere ratio, and for the flux weakening control, the d-axis current is modified to weaken the air-gap flux.

The reference speed value is the main input for the drive system, and the electromagnetic torque and rotor speed are the output. Two feedback loops, current or torque loop and speed loop, are added to provide desired performance. The output of the speed controller will be the reference value for the q-axis current while the d-axis current is set to zero. Both of the d- and q-axes currents are controlled to generate the torque and achieve the maximum efficiency drive. Figure 2.22 shows the implementation diagram of the typical FOC scheme, where the traditional PWM method is applied for the variable speed drive by the vectorial variable voltage and variable frequency control strategy.

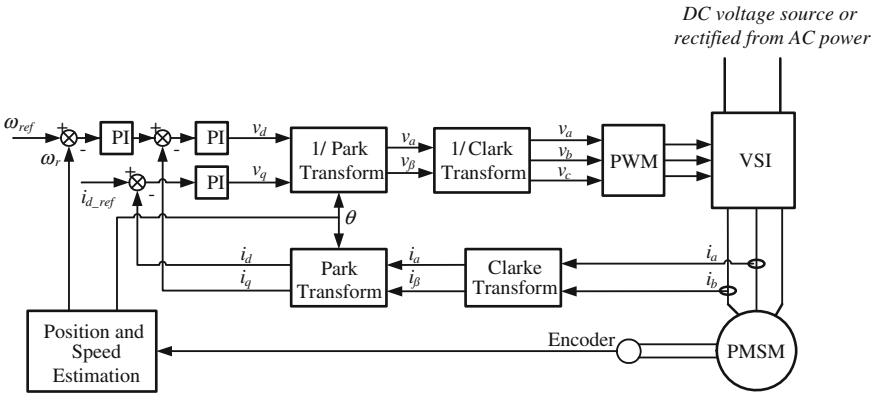

Fig. 2.22 Block diagram of FOC scheme for PMSM drive

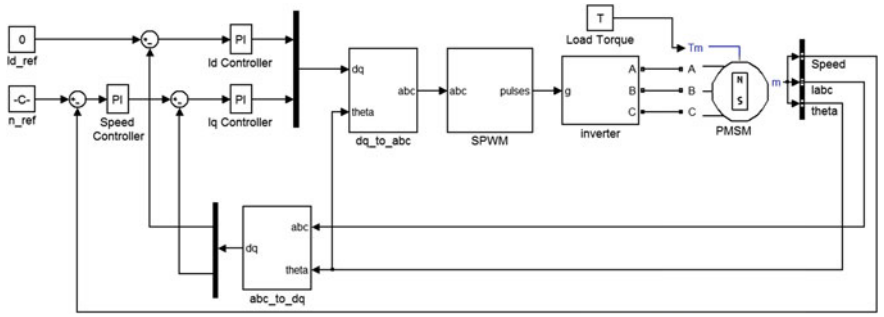

Fig. 2.23 Simulation block diagram of typical FOC based PMSM drive system

Similar to the six-step method, a simulation model of the FOC scheme based PMSM drive is built in MATLAB/SIMULINK. The sinusoidal back EMF machine model is selected from the SimPowerSystem tool box, in which the current sensors and rotor position sensor are integrated. The Park and Clark transformations are synthesized as one '*abc*_to_*dq*' block to transfer the variables between the stationary and rotating reference frames, as shown in Fig. 2.23. Two discrete PI controllers are used for the speed and current feedback loops.

The traditional triangulation PWM generation technique is applied. A triangular carrier wave sampling signal is compared directly with a sinusoidal modulating wave to determine the switching instants, and therefore the resultant pulse widths.

2.6.3 *Direct Torque Control*

In the DTC strategy, the flux linkage and torque are calculated in the two-phase stator reference frame, i.e., the α-β frame, which is transformed from the three-phase *a*-*b*-*c* reference frame by using the Clark transformation. The Clark transformation can be expressed in the matrix form as

$$\begin{bmatrix} \sigma_\alpha \\ \sigma_\beta \end{bmatrix} = \sqrt{\frac{2}{3}} \begin{bmatrix} 1 & -\frac{1}{2} & -\frac{1}{2} \\ 0 & \frac{\sqrt{3}}{2} & -\frac{\sqrt{3}}{2} \end{bmatrix} \begin{bmatrix} \sigma_a \\ \sigma_b \\ \sigma_c \end{bmatrix} \tag{2.34}$$

After the measured phase voltages and currents are transformed to the α-β frame, the flux linkage components of the α- and β-axes can be calculated as

$$\begin{cases} \lambda_\alpha = \int (v_\alpha - R_s i_\alpha) dt \\ \lambda_\beta = \int (v_\beta - R_s i_\beta) dt \end{cases} \tag{2.35}$$

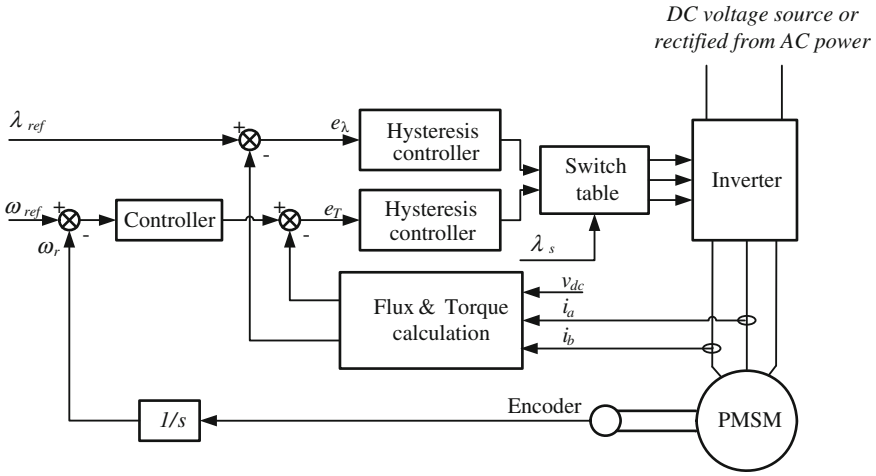

Fig. 2.24 Block diagram of typical DTC scheme based PMSM drive

The torque observer can then be designed as

$$T_e = \frac{3}{2} \cdot \frac{p_m}{2} \left(\lambda_\alpha i_\beta - \lambda_\beta i_\alpha \right) \tag{2.36}$$

Figure 2.24 shows the block diagram of a typical DTC scheme for PMSM drive. Two hysteresis controllers are applied to the flux linkage and torque control loops. The calculated flux linkage is also sent to the switching table to identify the current flux vector position.

From (2.35), the stator flux linkage is

$$\lambda_s = \int (v_s - R_s i_s) dt \tag{2.37}$$

where v_s and i_s are the stator voltage and current spatial vectors, respectively.

In the case of a PMSM, λ_s always varies even when the zero voltage vectors are applied because of the rotating rotor magnets, and thus, zero voltage vectors are not used for DTC driven PMSM. λ_s should always be in motion with respect to the rotor flux.

According to (2.36), the electromagnetic torque can be controlled effectively by controlling the amplitude and rotating speed of λ_s. For counter-clockwise operation, if the actual torque is smaller than the reference, the voltage vectors that keep λ_s rotating in the same direction are selected. The angle increases as fast as it can, and the actual torque increases as well. Once the actual torque is greater than the reference, the voltage vectors that keep λ_s rotating in the reverse direction are selected instead of the zero voltage vectors. The angle decreases, so does the torque. By selecting the voltage vectors in this way, λ_s will rotate all the time in the

Table 2.5 Switching table of typical DTC scheme for PMSM drive

Δe_λ	Δe_T	θ					
		θ_1	θ_2	θ_3	θ_4	θ_5	θ_6
1	1	$V_2(110)$	$V_3(010)$	$V_4(011)$	$V_5(001)$	$V_6(101)$	$V_1(100)$
	0	$V_6(101)$	$V_1(100)$	$V_2(110)$	$V_3(010)$	$V_4(011)$	$V_5(001)$
0	1	$V_3(010)$	$V_4(011)$	$V_5(001)$	$V_6(101)$	$V_1(100)$	$V_2(110)$
	0	$V_5(001)$	$V_6(101)$	$V_1(100)$	$V_2(110)$	$V_3(010)$	$V_4(011)$

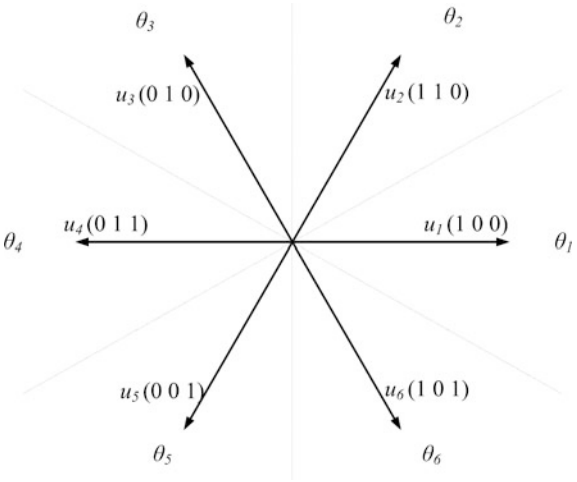

Fig. 2.25 Voltage vectors and spatial sector definition

direction determined by the output of the hysteresis controller for the torque. The switching table for controlling both the amplitude and rotating direction is shown in Table 2.5, in which the inverter voltage vector and spatial sector definitions are illustrated in Fig. 2.25.

Figure 2.26 shows the simulation model built based on the typical DTC scheme. The inverter switching status and DC bus voltage are utilized to calculate the stator voltage. The stator flux linkage is obtained in the observer. The traditional two-level hysteresis controllers are applied and the switching table is designed based on Table 2.5.

2.6.4 Model Predictive Control

The principle of MPC was introduced for industrial control applications in the 1970s after the publication of this strategy in the 1960s. The MPC requires great computational effort and it has been formerly limited to slowly varying systems, such as chemical processes. With the availability of inexpensive high computing

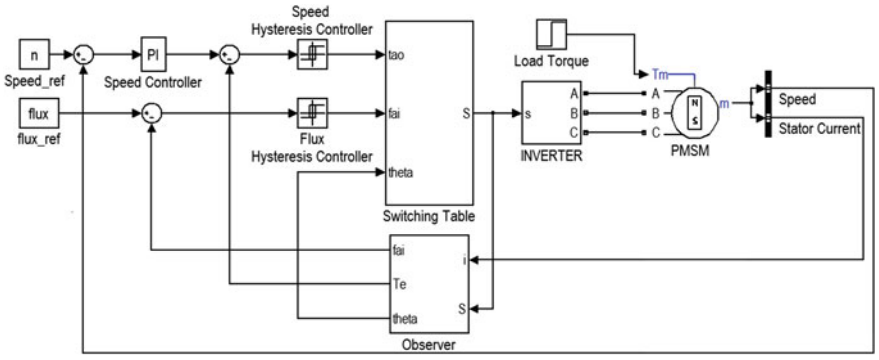

Fig. 2.26 Simulation block diagram of typical DTC based PMSM drive system

power microcomputers and modern digital control techniques, MPC is able to be applied to electrical drive systems [36, 55, 56].

Different from the employment of hysteresis comparators and the switching table in conventional DTC, the principle of vector selection in MPC is based on evaluating a defined cost function. The selected voltage vector from the conventional switching table in DTC may not necessarily be the best one for the purposes of torque and flux ripple reduction. Since there are limited discrete voltage vectors in the two-level inverter-fed PMSM drives, it is possible to evaluate the effects of each voltage vector and select the one minimizing the cost function.

The key technology of MPC lies in the definition of the cost function, which is related to the control objectives. The greatest concerns of PMSM drive applications are the torque and stator flux, and thus, the cost function is defined in such a way that both the torque and stator flux at the end of control period are as close as possible to the reference values. In this book, the cost function is defined as

$$\begin{aligned} \text{min:} \quad & G = |T_e^* - T_e^{k+1}| + k_1 \left| |\psi_s^*| - |\psi_s^{k+1}| \right| \\ & \text{s.t. } u_s^k \in \{V_0, V_1, \ldots, V_7\} \end{aligned} \tag{2.38}$$

where T_e^* and ψ_s^* are the reference torque and flux, T_e^{k+1} and ψ_s^{k+1} the predicted values of torque and flux, respectively, and k_1 is the weighting factor. Because the physical natures of electromagnetic torque and stator flux are different, the weighting factor k_1 is introduced to unify these terms. In this work, k_1 is selected to be T_n/ψ_n, where T_n and ψ_n are the rated values of torque and stator flux, respectively. It should be noted that when a null vector is selected, the specific state (V_0 or V_7) will be determined based on the principle of minimal switching commutations, which is related to the switching states of the previous voltage vector.

The voltage equations in the *d-q* reference frame are as follows:

$$u_d = R_s i_d + L_d \frac{di_d}{dt} - \omega L_q i_q \tag{2.39}$$

$$u_q = R_s i_q + L_q \frac{di_q}{dt} + \omega L_d i_d + \omega \psi_f \tag{2.40}$$

Given the voltage and current values at sampling instant k, the predicted current, torque and flux at instant $k + 1$ can be expressed as follows:

$$i_d^{k+1} = i_d^k + \frac{1}{L_d}\left(-R_s i_d^k + \omega^k L_q i_q^k + u_d^k\right) T_s \tag{2.41}$$

$$i_q^{k+1} = i_q^k + \frac{1}{L_q}\left(-\omega^k L_d i_d^k - R_s i_q^k + u_q^k - \omega^k \psi_f\right) T_s \tag{2.42}$$

$$\psi_s^{k+1} = \left(L_d i_d^{k+1} + \psi_f\right) + j L_q i_q^{k+1} \tag{2.43}$$

$$T_e^{k+1} = \frac{3}{2} p \psi_s^{k+1} i_s^{k+1} \tag{2.44}$$

where i_d^{k+1} and i_q^{k+1} are the predicted values of stator current for the sampling instant $k + 1$, T_s is the sampling period, T_e^{k+1} and ψ_s^{k+1} are the predicted values of torque and flux, respectively, which are also the main concerns for the cost function in the following MPC control scheme [1, 36, 49].

The block diagram of MPC is shown in Fig. 2.27. The inputs of the system are the reference and estimated values of torque and flux. By evaluating the effects of each voltage vector when applied to the machine, the voltage vector which minimizes the difference between the reference and predicted values is first selected, and then it is generated by the inverter.

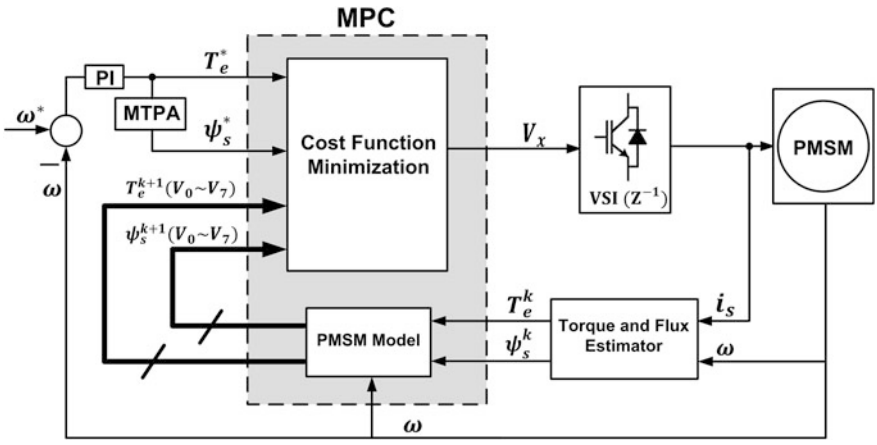

Fig. 2.27 Block diagram of MPC drive system in MATLAB/SIMULINK

2.6.4.1 One-Step Delay Compensation

The cost function in (2.38) assumes that all calculations and judgments are implemented at the *k*th instant and the selected vector will be applied immediately. However, in practical digital implementation, this assumption is not true and the applied voltage vector is not applied until the $(k + 1)$th instant.

In other words, for the duration between the *k*th and $(k + 1)$th instants, the applied rotor voltage vector u_s^k has been decided by the value in the $(k\text{-}1)$th instant and the evolutions of ψ_s and T_e for this duration are uncontrollable. What is left to be decided is actually the stator voltage vector u_s^{k+1}, which is applied at the beginning of the $(k + 1)$th instant. To eliminate this one step delay, the variables of ψ_s^{k+2} and T_e^{k+2} should be used rather than ψ_s^{k+1} and T_e^{k+1} for the evaluation of the cost function in (2.38). This fact is clearly illustrated in Fig. 2.28, where *x* indicates the state variables of a dynamic system and *u* is the input to be decided. For PMSM, *x* represents torque or stator flux value.

To eliminate the one-step delay in digital implementation, the cost function in (2.38) should be changed to (2.45) as shown below

$$\begin{aligned} \text{min:} \quad & G = |T_e^* - T_e^{k+2}| + k_1 \left| |\psi_s^*| - |\psi_s^{k+2}| \right| \\ & \text{s.t. } u_s^k \in \{V_0, V_1, \ldots, V_7\} \end{aligned} \tag{2.45}$$

Obtaining ψ_s^{k+2} and T_e^{k+2} in (2.45) requires a two-step prediction. To obtain the best voltage vector minimizing the cost function in (2.45), each possible configuration for u_e^{k+1} will be evaluated to obtain the value at the $(k + 2)$th instant.

2.6.4.2 Linear Multiple Horizon Prediction

A linear multiple horizon prediction formula is introduced in this section. This formula incorporates two formulas. The first one is the same as in (2.38). The linear

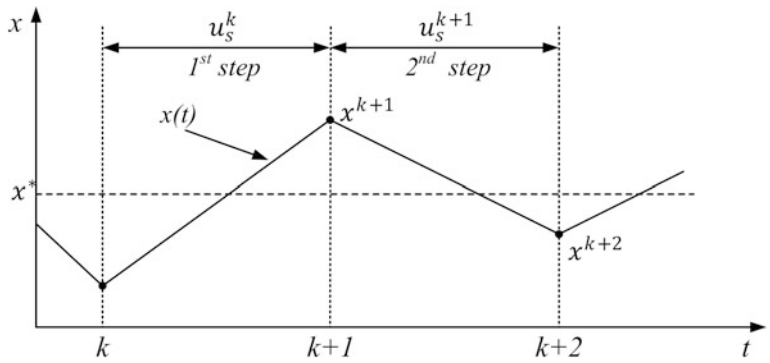

Fig. 2.28 One-step delay in digital control systems

multiple horizon prediction formula, which is multiplied by a factor A, considers the errors in the $(k + N)$th instant $(N > 1)$. Different from the model-based predictions for ψ_s^{k+1} and T_e^{k+1}, the stator flux and torque at the $(k + N)$th instant are predicted from the value at the kth and $(k + 1)$th instants using linear extrapolations, which are expressed as

$$T_e^{k+N} = T_e^k + (N-1)(T_e^{k+1} - T_e^k) \tag{2.46}$$

$$|\psi_s^{k+N}| = \left||\psi_s^k| + (N-1)\left||\psi_s^{k+1}| - |\psi_s^k|\right|\right| \tag{2.47}$$

The expression of the proposed cost function is

$$\begin{aligned} \text{min:}\quad G = {} & |T_e^* - T_e^{k+1}| + k_1\left||\psi_s^*| - |\psi_s^{k+1}|\right| \\ & + A\left(|T_e^* - T_e^{k+N}| + k_1\left||\psi_s^*| - |\psi_s^{k+N}|\right|\right) \quad s.t.\, u_s^k \in \{V_0, V_1, \ldots, V_7\} \end{aligned} \tag{2.48}$$

2.6.5 Numerical and Experimental Comparisons of DTC and MPC

2.6.5.1 Numerical Simulation

In this section, the simulation tests of DTC and MPC are carried out by using Matlab/Simulink. The parameters of the motor are listed in Table 2.6. The sampling frequency of both methods is set to 5 kHz. The values of control parameters are $k_1 = 25.4$, $A = 0.1$, and $N = 10$ [36].

This simulation test combines start-up, steady-state and external load tests. The motor starts up from 0 s with several reference speeds (500 rev/min, 1000 rev/min, 1500 rev/min and 2000 rev/min). After reaching the reference speed, the motor maintains the speed for at least 0.2 s and an external load is applied at 0.3 s. Figures 2.29, 2.30, 2.31 and 2.32 show the combined load test for four control strategies for one reference speed, 1000 rev/min. From top to bottom, the curves are the stator current, stator flux, torque, motor speed, and switching frequency, respectively. The test results for other speed situations can be found in [36].

Table 2.6 Motor parameters

Number of pole pairs	p	3
Permanent magnet flux	ψ_f	0.1057 Wb
Stator resistance	R_s	1.8 Ω
d- and q-axis inductance	L_d, L_q	15 mH
Rated torque	T_N	4.5 Nm
DC bus voltage	V_{dc}	200 V

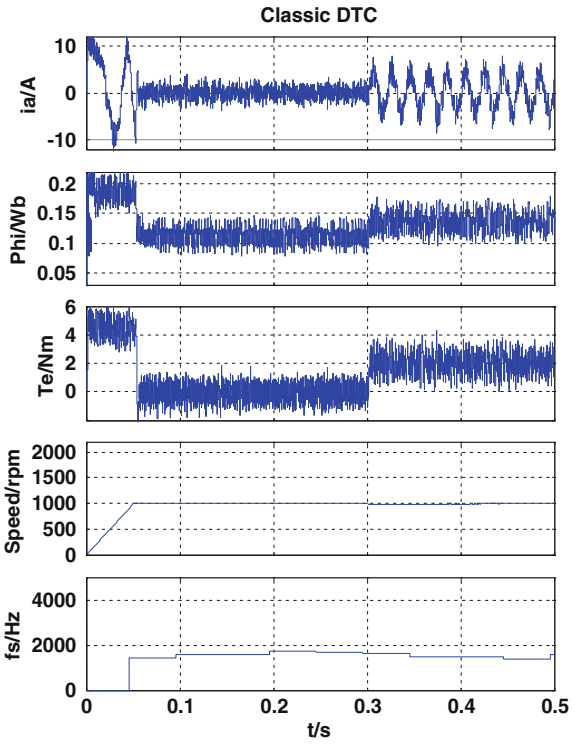

Fig. 2.29 Combined load test for DTC

By comparing Fig. 2.30 with Fig. 2.29, it is shown that the torque and flux ripples of MPC are lower than that of DTC. In Fig. 2.31, MPC with one-step delay compensation (indicated as MPC + comp) presents torque and flux ripples even lower than MPC along with an increase in switching frequency. Figure 2.32 illustrates the responses by using cost function (2.48), where factor A is included in the simulation. As shown, the introduction of linear multiple horizon prediction (factor A, and indicated as MPC + A) can greatly reduce the switching frequency only with a quite limited degradation of torque and flux ripples. As shown, all these methods present similar dynamic performance and the motor can reach the reference speed rapidly. When the load was applied, the motor speed returned to its original value in a very short time period.

The recorded data from 0.1 to 0.3 s are picked to calculate the torque and flux ripples (obtained by standard deviations). The torque and flux ripples of these control methods are summarized in Table 2.7. A segment (three periods) of the stator current of phase A is used to calculate the total harmonic distortion (THD) and current harmonic spectrum.

As shown, MPC can achieve lower torque ripple than that of DTC as proven. However, MPC's characteristic in flux ripple reduction is quite unstable. With the help of one-step delay compensation, the steady-state performance of MPC is

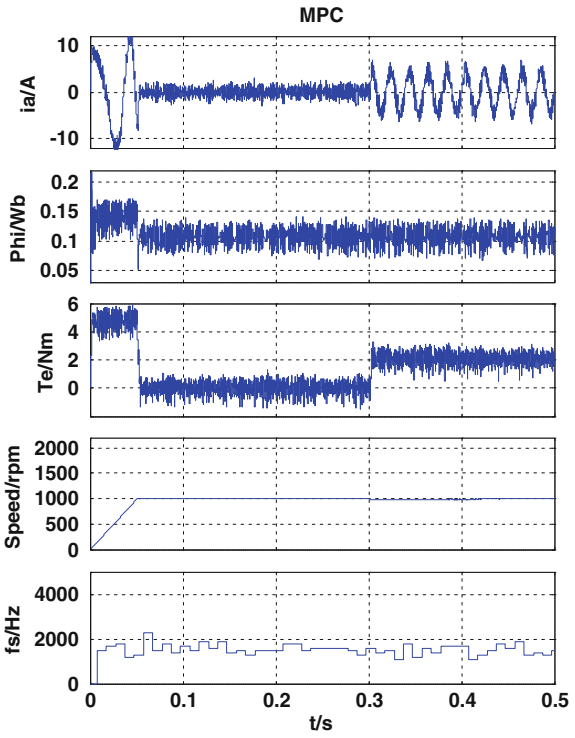

Fig. 2.30 Combined load test for MPC

improved significantly. It should be noticed that the switching frequency has increased by almost two times in most tests when one-step delay is compensated. The introduction of linear multiple horizon prediction can effectively reduce the switching frequency and flux ripple. However, its ability on torque ripple reduction is quite insignificant.

2.6.5.2 Experimental Testing

In addition to the simulation study, the control methods mentioned above are further experimentally tested on a two-level inverter-fed PMSM motor drive. The experimental setup is illustrated in Fig. 2.33. A dSPACE DS1104 PPC/DSP control board is employed to implement the real-time algorithm coding using C language. A three phase intelligent power module equipped with an insulated-gate bipolar transistor (IGBT) is used as an inverter. The gating pulses are generated in the DS1104 board and then sent to the inverter. The load is applied using a programmable dynamo-meter controller DSP6000 (Fig. 2.34). A 2500-pulse incremental encoder is equipped to obtain the rotor speed of PMSM. All experimental results are recorded by the ControlDesk interfaced with DS1104 and PC at 5 kHz sampling frequency [36].

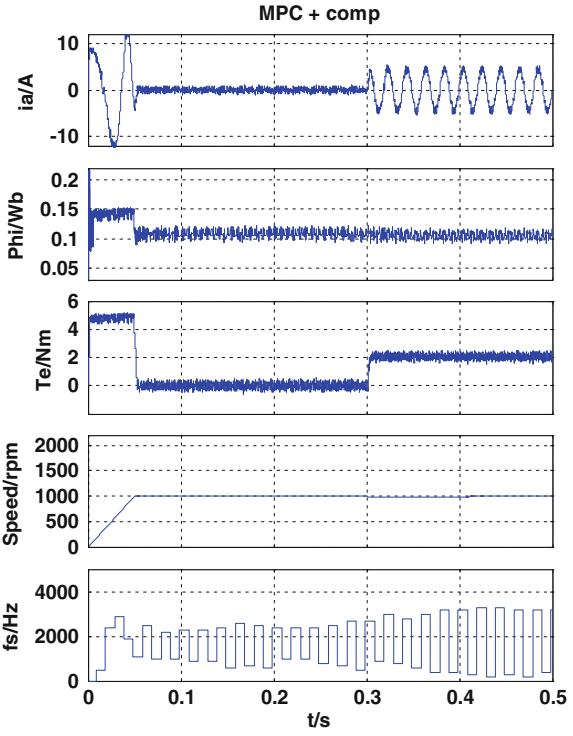

Fig. 2.31 Combined load test for MPC with one-step delay compensation

The steady-state responses at 1000 rpm are presented in this section. From top to bottom, the curves shown are torque, stator flux and switching frequency, respectively.

Figures 2.35 and 2.36 show the measured steady-state performance at 1000 rpm. It is seen that the implementation of MPC can reduce the torque ripple, but does not reduce the flux ripple. When the one-step delay is compensated, a significant decrease of torque and flux ripples can be found as well as an obvious increase of switching frequency. When the linear multiple horizon prediction is added to MPC, it can be seen that the torque and flux ripples are slightly decreased along with a limited reduction of the switching frequency.

Table 2.8 lists the torque and flux ripples of these control methods in experiment. As shown, similar conclusions can be obtained as those from Table 2.7. According to the analysis above, it can be concluded that:

(1) MPC can achieve lower torque ripple than that of DTC whilst maintaining/reducing the switching frequency as proven in both simulation and experimental tests. However, MPC's ability in flux ripple reduction is insignificant and even unstable.

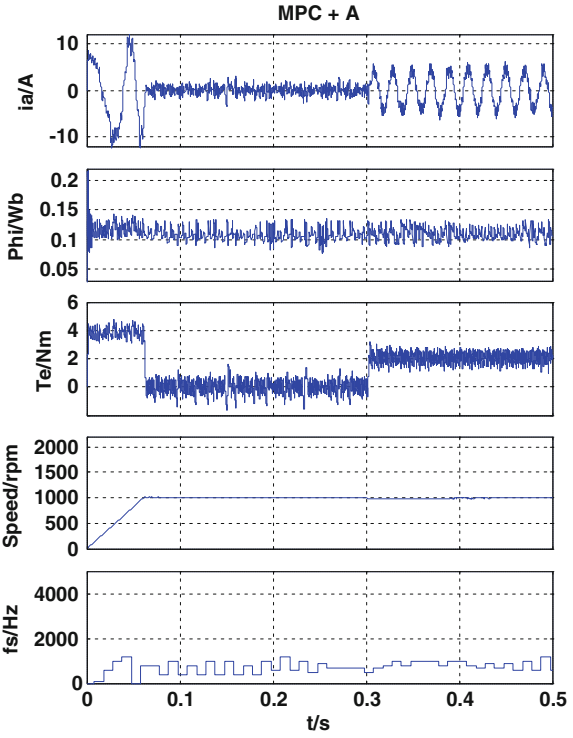

Fig. 2.32 Combined load test for MPC with linear multiple horizon prediction

Table 2.7 Steady-state response (simulation)

Method	THD (%)	f_{av} (kHz)	ψ_{rip}(Wb)	T_{rip}(Nm)
DTC	28.83	1.5972	0.0155	0.6869
MPC	18.55	1.5692	0.0138	0.4952
MPC + comp	8.17	1.5812	0.0059	0.2253
MPC + A	15.52	0.6640	0.0090	0.5102

(2) When one-step delay is compensated, the steady-state performance of MPC in terms of torque and flux ripples reduction is significantly improved. It should be noticed that the performance improvement also comes with a remarkable switching frequency increase (two times or more).

(3) By introducing linear multiple horizon prediction to MPCs, a significant switching frequency reduction can be found as well as an obvious decrease in flux ripple. However, it comes with heavy penalty of torque ripple increasing, especially at low motor speed.

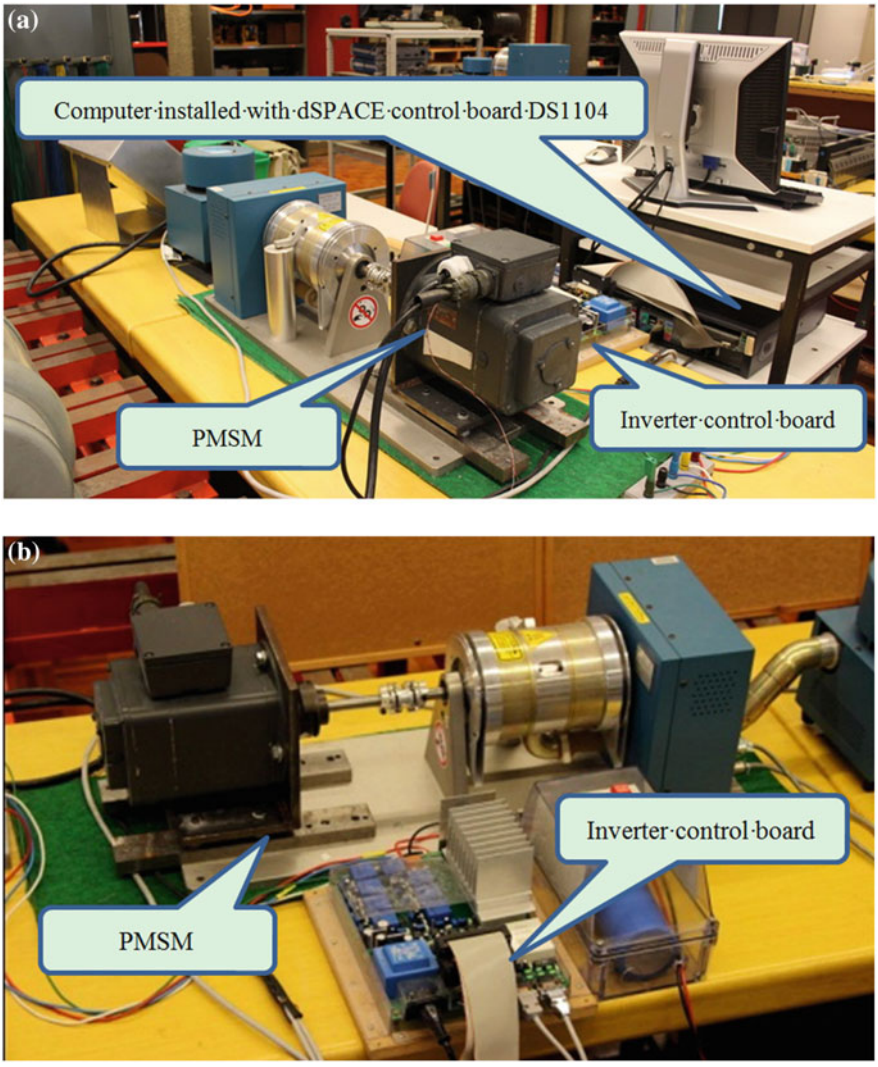

Fig. 2.33 Experimental setup of testing system: **a** overview of the testing platform and **b** front view of the PMSM and inverter control board

2.6.6 Improved MPC with Duty Ratio Optimization

There are many improvements for these control algorithms. One of them known as MPC with duty ratio optimization will be selected for the control of PM-SMC TFM. As a general algorithm, the theory and test results will be presented in this section.

Fig. 2.34 Dynamo-meter controller DSP6000

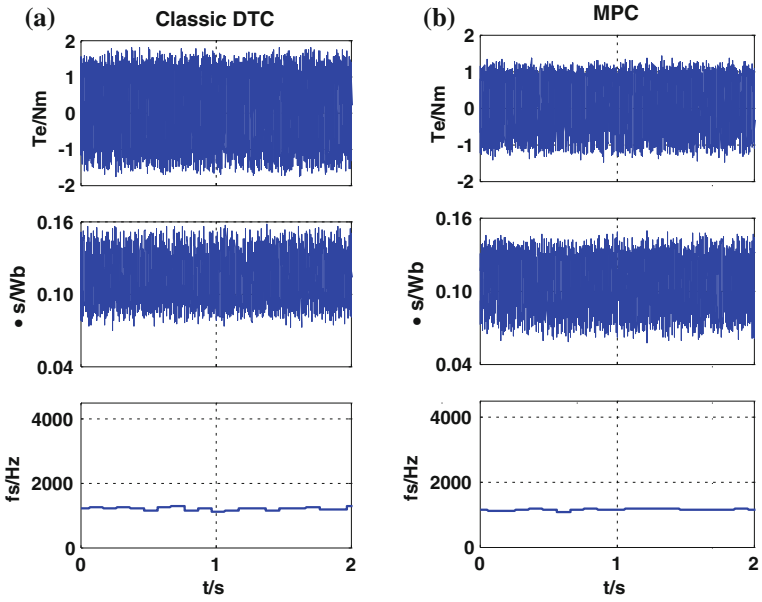

Fig. 2.35 Steady-state response for: **a** DTC, **b** MPC

In the conventional MPC, the selected voltage vector works during the whole sampling period. In many cases, it is not necessary to work for the entire period to meet the performance requirement of torque and flux. This is one of the main reasons for the torque and flux ripples. By introducing a null vector to each sampling period, the effects of voltage on torque can be adjusted to be more moderate, in order to diminish the ripples of torque and flux.

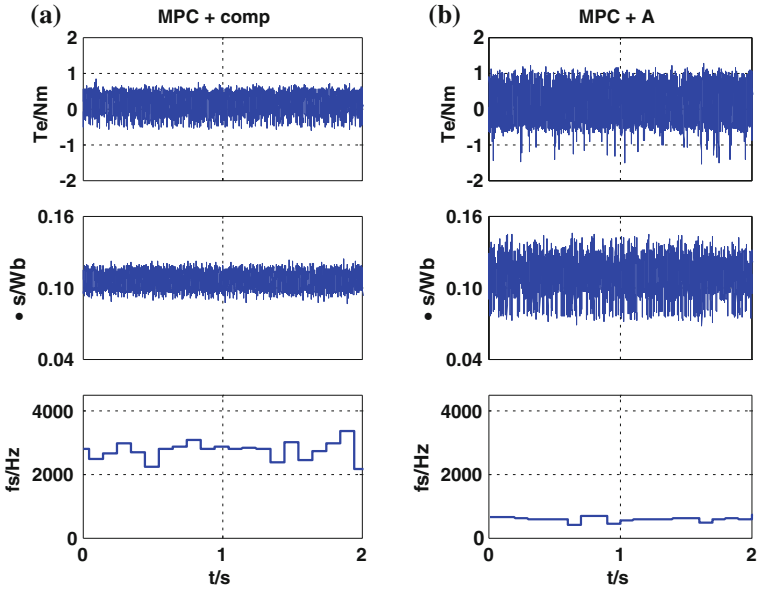

Fig. 2.36 Steady-state response for: **a** MPC with one-step delay compensation, and **b** MPC with linear multiple horizon prediction

Table 2.8 Steady-state response at 1000 rpm (experimental)

Method	f_{av} (kHz)	ψ_{rip}(Wb)	T_{rip}(Nm)
DTC	1.2129	0.0167	0.8446
MPC	1.1393	0.0173	0.6394
MPC + comp	2.7335	0.0056	0.2310
MPC + A	0.6045	0.0136	0.4460

Actually, the torque can be changed by adjusting the amplitude and time duration of u_s. The amplitude is decided by the DC bus voltage and is usually fixed, while the time duration of u_s can be varied from zero to the whole period, which is equivalent to changing the voltage vector length. The null vector only decreases the torque, while appropriate non-zero vectors can increase the torque, and it is possible to employ both null and nonzero vectors during one cycle to reduce the torque ripple. The appropriate non-zero vectors are also referred as 'active vector'. The key issue is how to determine the time duration of the two vectors, or the duty ratio of the active vector.

The expression of duty ratio for MPC is shown as follows

$$d = \left|\frac{T_e^* - T_e^{k+1}}{C_T}\right| + \left|\frac{\psi_s^* - \psi_e^{k+1}}{C_\psi}\right|, \tag{2.49}$$

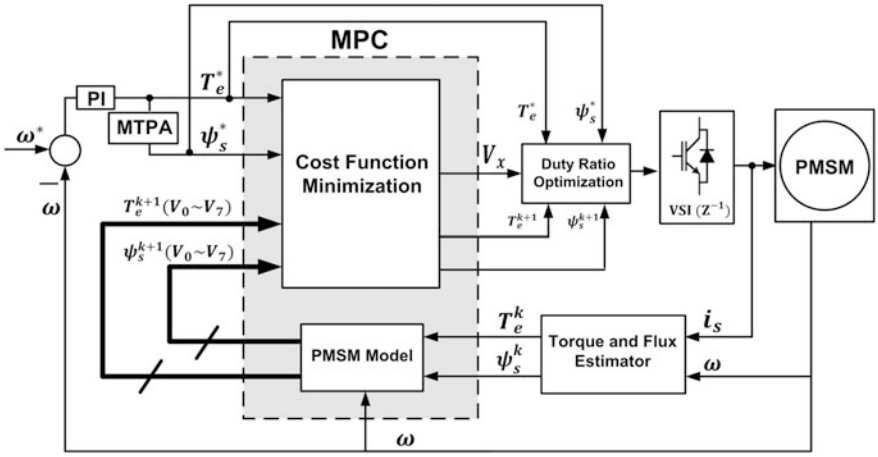

Fig. 2.37 Diagram of an improved MPC with duty ratio optimization in MATLAB/SIMULINK

where d is the duty ratio of the active voltage vector, and C_T and C_ψ are two positive parameters. The idea of this method is that the larger the difference between the reference and predicted torque values, the larger is the duty ratio value [36]. On the other hand, the lower the C_T and C_ψ values, the quicker is the dynamic response (e.g. take less time to reach the given speed), but the poorer will be the steady-state response (e.g. higher torque and flux ripples). Higher values of C_T and C_ψ could lead to better steady-state responses, but slower dynamic responses. Therefore, the determination of these values is a compromise between the steady-state and dynamic performances. Extensive simulation and experimental results have proven that the PM flux value and half-rated torque value for C_T and C_ψ can provide a good compromise between the steady state performance and the dynamic response. The block diagram of the proposed improved MPC is shown in Fig. 2.37.

2.6.7 Numerical and Experimental Comparisons of DTC and MPC with Duty Ratio Optimization

2.6.7.1 Numerical Simulation

The parameters of the motor and control system simulated in this section are listed in Table 2.9. Similar to the previous test example, this simulation test combines the start-up, steady-state and external load tests. The motor starts up from 0 s with several reference speeds (500 rev/min, 1000 rev/min, 1500 rev/min and 2000 rev/min). After reaching the reference speed, the motor maintains the speed for at least 0.2 s and an external load is applied at 0.3 s. Figure 2.38 shows the combined load test for one reference speed, 1000 rev/min. From top to bottom, the curves are

Table 2.9 Motor and control system parameters

Parameter	Symbol	Value
Number of pole pairs	p	3
Permanent magnet flux	ψ_f	0.1057 Wb
Stator resistance	R_s	1.8 Ω
d-axis and q-axis inductance	L_d, L_q	15 mH
DC bus voltage	V_{dc}	200 V
Inertia	J	0.002 kg · m^2
Torque constant gain	C_T	2
Flux constant gain	C_ψ	0.1
Sampling frequency	f_{sp}	5 kHz

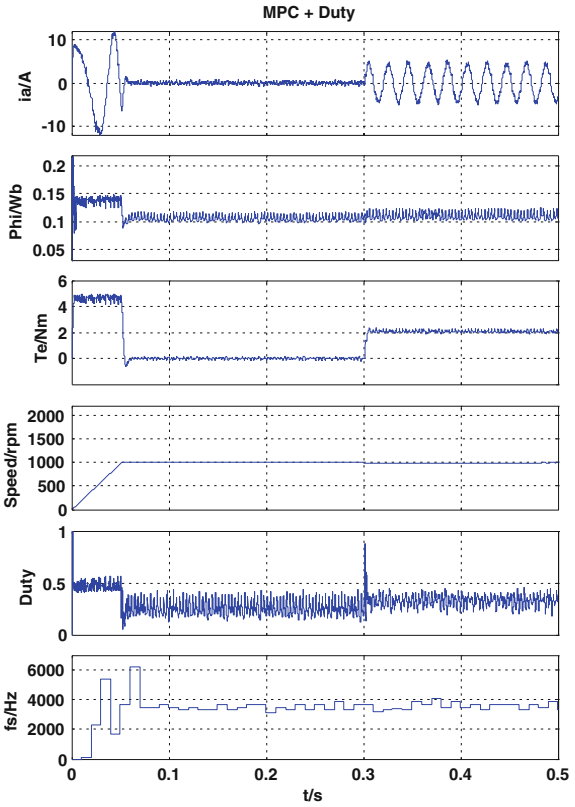

Fig. 2.38 Combined load test for MPC with duty ratio optimization at 1000 rev/min

the stator current, stator flux, torque, motor speed, and switching frequency, respectively. The test results for other speed situations can be found in [36].

It can be found that the proposed MPC scheme present very low torque and flux ripples and excellent dynamic response. The proposed MPC scheme also presents very low stator current THDs and narrow harmonic spectrums with the dominant harmonics of around 5 kHz.

2.6.7.2 Experimental Test

The experimental tests are performed on the same testing platform introduced in the last section. Figure 2.39 shows the steady-state responses at 1000 rpm for three control strategies, namely (a) DTC, (b) MPC, and (c) MPC with duty ratio optimization.

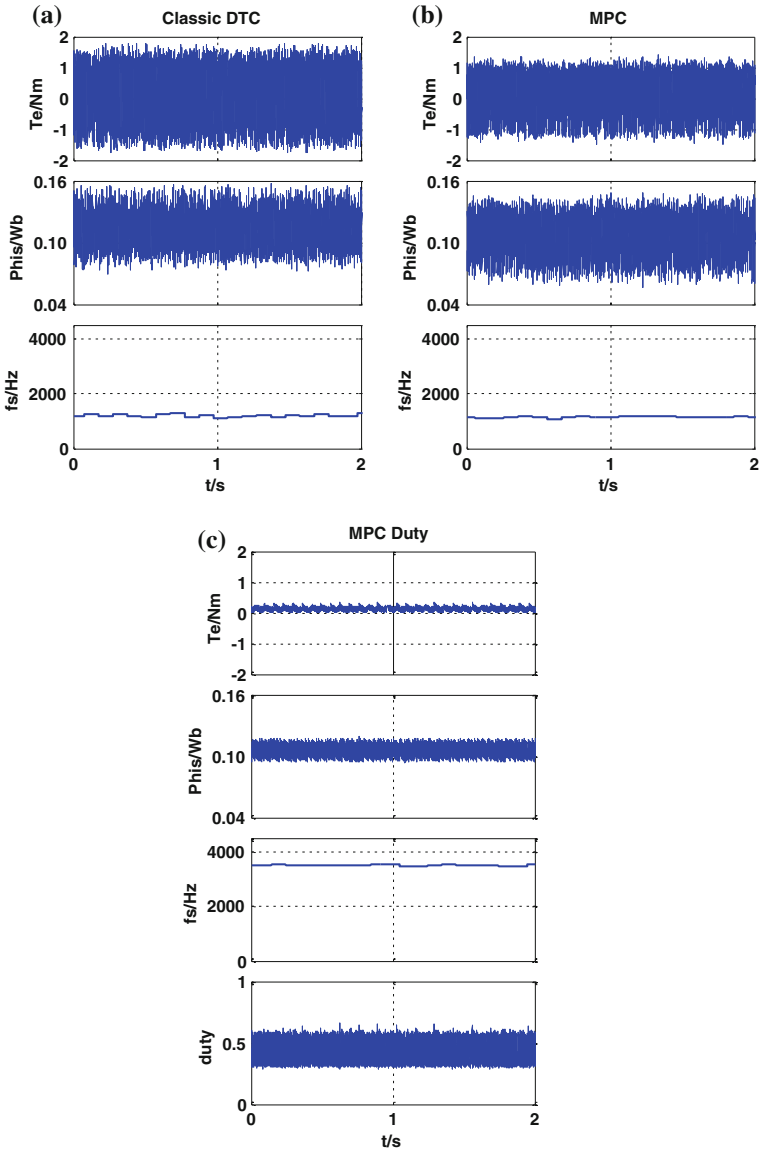

Fig. 2.39 Steady-state response at 1000 rpm for: **a** DTC, **b** MPC and **c** MPC with duty ratio optimization

It can be seen that in MPC with duty ratio optimization, the torque and flux ripples are reduced significantly compared to other methods. The duty ratio increases along with the increase in motor speed.

According to the analysis above, it can be concluded that:

(1) MPC with duty ratio optimization can achieve a better performance than DTC and original MPC in terms of torque and flux ripples reduction;
(2) Under the same system sampling frequency (5 kHz), the switching frequency of the improved method is much higher than other methods; and
(3) In DTC and MPC, the switching frequency slightly decreases along with the increase of motor speed. However, the switching frequency is almost stable in the proposed method.

More experimental results including different speed, dynamic response and data analysis can be found in [36].

2.7 Summary

This chapter presents the multi-disciplinary design analysis models and methods for electrical machines and drive systems. All the models and methods are discussed in terms of the three major parts of electrical drive systems, namely electrical machines, power electronic converters and controllers. Electromagnetic, thermal and mechanical analyses based on different models, e.g. FEM, have been investigated for the design of electrical machines with several prototypes developed in our research center. Various kinds of popular control algorithms have been described for the controller design. Several examples investigated in our previous work have been presented to show the effectiveness of the proposed models and analysis methods.

References

1. Lei G, Wang TS, Guo YG, Zhu JG, Wang SH (2014) System level design optimization methods for electrical drive systems: deterministic approach. IEEE Trans Ind Electron 61 (12):6591–6602
2. Lei G, Wang TS, Zhu JG, Guo YG, Wang SH (2015) System level design optimization method for electrical drive system: robust approach. IEEE Trans Ind Electron 62(8):4702–4713
3. Zhu JG, Guo YG, Lin ZW, Li YJ, Huang YK (2011) Development of PM transverse flux motors with soft magnetic composite cores. IEEE Trans Magn 47(10):4376–4383
4. Zhu JG, Ramsden VS (1998) Improved formulations for rotational core losses in rotating electrical machines. IEEE Trans Magn 34(4):2234–2242
5. Guo YG, Zhu JG, Lu HY, Lin ZW, Li YJ (2012) Core loss calculation for soft magnetic composite electrical machines. IEEE Trans Magn 48(11):3112–3115

6. Guo YG, Zhu JG, Lu HY, Li YJ, Jin JX (2014) Core loss computation in a permanent magnet transverse flux motor with rotating fluxes. IEEE Trans Magn 50(11). Article#: 6301004
7. Guo YG, Zhu JG, Zhong JJ, Wu W (2003) Core losses in claw pole permanent magnet machines with soft magnetic composite stators. IEEE Trans Magn 39(5):3199–3201
8. Huang YK, Zhu JG, Guo YG, Lin ZW, Hu Q (2007) Design and analysis of a high speed claw pole motor with soft magnetic composite core. IEEE Trans Magn 43(6):2492–2494
9. Huang YK, Zhu JG et al (2009) Thermal analysis of high-speed SMC motor based on thermal network and 3-D FEA with rotational core loss included. IEEE Trans Magn 45(10):4680–4683
10. Pfister P-D, Perriard Y (2010) Very-high-speed slotless permanent-magnet motors: analytical modeling, optimization, design, and torque measurement methods. IEEE Trans Ind Electron 57(1):296–303
11. Komeza K, Dems M (2012) Finite-element and analytical calculations of no-load core losses in energy-saving induction motors. IEEE Trans Ind Electron 59(7):2934–2946
12. Wang SH, Meng XJ, Guo NN, Li HB, Qiu J, Zhu JG et al (2009) Multilevel optimization for surface mounted PM machine incorporating with FEM. IEEE Trans Magn 45(10):4700–4703
13. Barcaro M, Bianchi N, Magnussen F (2012) Permanent-magnet optimization in permanent-magnet-assisted synchronous reluctance motor for a wide constant-power speed range. IEEE Trans Ind Electron 59(6):2495–2502
14. Vese I, Marignetti F, Radulescu MM (2010) Multiphysics approach to numerical modeling of a permanent-magnet tubular linear motor. IEEE Trans Ind Electron 57(1):320–326
15. Bornschlegell AS, Pelle J, Harmand S, Fasquelle A, Corriou J-P (2013) Thermal optimization of a high-power salient-pole electrical machine. IEEE Trans Ind Electron 60(5):1734–1746
16. Lee D-H, Pham TH, Ahn J-W (2013) Design and operation characteristics of four-two pole high-speed SRM for torque ripple reduction. IEEE Trans Ind Electron 60(9):3637–3643
17. Flieller D, Nguyen NK, Wira P, Sturtzer G, Abdeslam DO, Merckle J (2014) A self-learning solution for torque ripple reduction for nonsinusoidal permanent-magnet motor drives based on artificial neural networks. IEEE Trans Ind Electron 61(2):655–666
18. Hasanien HM, Abd-Rabou AS, Sakr SM (2010) Design optimization of transverse flux linear motor for weight reduction and performance improvement using response surface methodology and genetic algorithms. IEEE Trans Energy Convers 25(3):598–605
19. Hasanien HM (2011) Particle swarm design optimization of transverse flux linear motor for weight reduction and improvement of thrust force. IEEE Trans Ind Electron 58(9):4048–4056
20. Lei G, Liu CC, Guo YG, Zhu JG (2015) Multidisciplinary design analysis for PM motors with soft magnetic composite cores. IEEE Trans Magn 51(11). Article 8109704
21. Hua W, Cheng M, Zhu ZQ, Howe D (2006) Design of flux-switching permanent magnet machine considering the limitation of inverter and flux-weakening capability. In: Proceedings of 41st IAS annual meeting-industry applications conference, vol 5, pp 2403–2410
22. Liu CC, Zhu JG, Wang YH, Lei G, Guo YG, Liu XY (2014) A low-cost permanent magnet synchronous motor with SMC and ferrite PM. In: Proceedings of 17th international conference on electrical machines and systems (ICEMS), pp 397–400
23. Fei W, Luk PCK, Shen JX, Wang Y, Jin M (2012) A novel permanent-magnet flux switching machine with an outer-rotor configuration for in-wheel light traction applications. IEEE Trans Ind Appl 48(5):1496–1506
24. Guo YG (2003) Development of low cost high performance permanent magnet motors using new soft magnetic composite materials, UTS thesis (PhD)
25. Guo YG, Zhu JG, Watterson PA, Wei Wu (2006) Development of a PM transverse flux motor with soft magnetic composite core. IEEE Trans Energy Conver 21(2):426–434
26. Guo YG, Zhu JG, Watterson PA, Wei Wu (2003) Comparative study of 3-D flux electrical machines with soft magnetic composite cores. IEEE Trans Ind Appl 39(6):1696–1703
27. Guo YG, Zhu JG, Dorrell D (2009) Design and analysis of a claw pole PM motor with molded SMC core. IEEE Trans Magn 45(10):582–4585
28. Lei G, Shao KR, Guo YG, Zhu JG (2012) Multi-objective sequential optimization method for the design of industrial electromagnetic devices. IEEE Trans Magn 48(11):4538–4541

29. Lei G, Guo YG, Zhu JG et al (2012) System level six sigma robust optimization of a drive system with PM transverse flux machine. IEEE Trans Magn 48(2):923–926
30. Lei G, Zhu JG, Guo YG, Hu JF, Xu W, Shao KR (2013) Robust design optimization of PM-SMC motors for Six Sigma quality manufacturing. IEEE Trans Magn 49(7):3953–3956
31. Lei G, Zhu JG, Guo YG, Shao KR, Xu W (2014) Multiobjective sequential design optimization of PM-SMC motors for six sigma quality manufacturing. IEEE Trans Magn, 50 (2). Article 7017704
32. Liu CC, Zhu JG, Wang YH, Guo YG, Lei G, Liu XY (2015) Development of a low-cost double rotor axial flux motor with soft magnetic composite and ferrite permanent magnet materials. J Appl Phys, 117(17). Article # 17B507
33. Teng QF, Zhu JG, Wang TS, Lei G (2012) Fault tolerant direct torque control of three-phase permanent magnet synchronous motors. WSEAS Trans Syst 8(11):465–476
34. Teng QF, Bai J, Zhu JG, Sun Y (2013) Fault tolerant model predictive control of three-phase permanent magnet synchronous motors. WSEAS Trans Syst 12(8):385–397
35. Wang Y (2011) Investigation of rotor position detection schemes for PMSM drives based on analytical machine model incorporating nonlinear saliencies, UTS thesis (PhD)
36. Wang TS (2013) Model predictive torque control of PMSM with duty ratio optimization for torque ripple reduction, UTS thesis (Master degree)
37. Kim SY, Lee W, Rho MS, Park SY (2010) Effective dead-time compensation using a simple vectorial disturbance estimator in PMSM drives. IEEE Trans Ind Electron 57(5):1609–1614
38. Lee J, Hong J, Nam K, Ortega R, Praly L, Astolfi A (2010) Sensorless control of surface-mount permanent-magnet synchronous motors based on a nonlinear observer. IEEE Trans Power Electron 25(2):290–297
39. Genduso F, Miceli R, Rando C, Galluzzo GR (2010) Back EMF sensorless-control algorithm for high-dynamic performance PMSM. IEEE Trans Ind Electron 57(6):2092–2100
40. Takahashi I, Noguchi T (1986) A new quick-response and high-efficiency control strategy of an induction motor. IEEE Trans Ind Appl 22(5):820–827
41. Depenbrock M (1988) Direct self-control (DSC) of inverter-fed induction machine. IEEE Trans Power Electron 3(4):420–429
42. Buja GS, Kazmierkowski MP (2004) Direct torque control of PWM inverter-fed AC motors-A survey. IEEE Trans Ind Electron 51(4):744–757
43. Lai YS, Chen JH (2001) A new approach to direct torque control of induction motor drives for constant inverter switching frequency and torque ripple reduction. IEEE Trans Energy Convers 16(3):220–227
44. Lascu C, Trzynadlowski A (2004) A sensorless hybrid DTC drive for high-volume low-cost applications. IEEE Trans Ind Electron 51(5):1048–1055
45. Zhang Y, Zhu J, Xu W, Hu J, Dorrell DG, Zhao Z (2010) Speed sensorless stator flux oriented control of three-level inverter-fed induction motor drive based on fuzzy logic and sliding mode control. In: Proceedings of 36th IEEE IECON, pp 2926–293
46. Zhang Y, Zhu J (2011) Direct torque control of permanent magnet synchronous motor with reduced torque ripple and commutation frequency. IEEE Trans Power Electron 26(1):235–248
47. Zhang Y, Zhu J (2011) A novel duty cycle control strategy to reduce both torque and flux ripples for DTC of permanent magnet synchronous motor drives with switching frequency reduction. IEEE Trans Power Electron 26(10):3055–3067
48. Zhang Y, Zhu J, Xu W, Guo Y (2011) A simple method to reduce torque ripple in direct torque-controlled permanent-magnet synchronous motor by using vectors with variable amplitude and angle. IEEE Trans Ind Electron 58(7):2848–2859
49. Wang TS, Zhu JG, Zhang YC (2011) Model predictive torque control for PMSM with duty ratio optimization. In Proceedings of 2011 international conference on electrical machines and systems (ICEMS), pp 1–5, 20–23 August 2011
50. Miranda H, Cortes P, Yuz J, Rodriguez J (2009) Predictive torque control of induction machines based on state-space models. IEEE Trans Ind Electron 56(6):1916–1924
51. Geyer T, Papafotiou G, Morari M (2009) Model predictive direct torque control—Part I: Concept, algorithm, and analysis. IEEE Trans Ind Electron 56(6):1894–1905

52. Kouro S, Cortes P, Vargas R, Ammann U, Rodriguez J (2009) Model predictive control—a simple and powerful method to control power converters. IEEE Trans Ind Electron 56 (6):1826–1838
53. Morel F, Retif J-M, Lin-Shi X, Valentin C (2008) Permanent magnet synchronous machine hybrid torque control. IEEE Trans Ind Electron 55(2):501–511
54. Drobnic K, Nemec M, Nedeljkovic D, Ambrozic V (2009) Predictive direct control applied to AC drives and active power filter. IEEE Trans Ind Electron 56(6):1884–1893
55. Zhang Y, Xie W (2014) Low complexity model predictive control-single vector-based approach. IEEE Trans Power Electron 29(10):5532–5541
56. Zhang Y, Qu C (2015) Model predictive direct power control of PWM rectifiers under unbalanced network conditions. IEEE Trans Ind Electron 62(7):4011–4022

http://www.springer.com/978-3-662-49269-7

Multidisciplinary Design Optimization Methods for Electrical Machines and Drive Systems

Lei, G.; Zhu, J.; Guo, Y.

2016, XIV, 241 p. 151 illus., 95 illus. in color., Hardcover
ISBN: 978-3-662-49269-7